Simulation and Analysis of a Metamaterial Filter on a Flexible Liquid Crystal Polymer Substrate

by

Udarius Lamon Blair

A thesis submitted to the Graduate Faculty of
Auburn University
In partial fulfillment of the
Requirements for the Degree of

Master of Science in Electrical Engineering

Auburn, Alabama
May 4, 2014

Keywords: Metamaterials, CSRR, LCP, HFSS, Filter

Approved by

Robert Dean, Chair, Associate Professor of Electrical and Computer Engineering
Stuart Wentworth, Associate Professor of Electrical and Computer Engineering
Lloyd Riggs, Professor of Electrical and Computer Engineering

Abstract

Since 1968 there has been an ever increasing interest in the study of metamaterials. These man-made substances have tremendous potential to change the scientific study of optics, communications, and the overall RF regime. Several types of structures have been proposed to realize metamaterials, but none more common than the split ring resonator and the complementary split ring resonator. Using the capabilities of the complementary split ring resonator coupled to a single-ended microstrip transmission line can yield a myriad of wide-band filtering affects across a designed frequency range. These filters include stop band, high pass, and band pass configurations. When combined with a flexible substrate, these filters further progress the optical studies of metamaterial filters.

Evaluating these filters without fabrication requires a powerful simulation tool. Ansys's High Frequency Structure Simulator (HFSS) is such a tool. With it, the aforementioned filters were designed and analyzed. A liquid crystal polymer (LCP) substrate made it possible to design both planar filters and filters bent around a specified radius of curvature. The purpose of this thesis is to compare and analyze the scattering parameters of the planar structures to the curved structures in hopes they will produce similar results. Wide-band filters with consistent behavior across various degrees of inflection have the potential to propel metamaterials research into a new era.

Acknowledgments

The author would like to thank his mentors, family, and friends for their unwavering support throughout his academic tenure at Auburn University: Dr. Robert Dean for guidance and instruction, Dr. Lloyd Riggs, Dr. Robert Nelms, Dr. Stuart Wentworth and Mr. Jim Killian for their sound advice and help when it was needed most, his mother Cynthia Blair, his grandmother Mary Blair, his sister BreAnna McDonel, his aunt Martha Shepherd, his uncle Kenny Blair, his aunt Laretha Todd, his aunt Amanda Lampley, and his uncle Nicarlto Oliver for being his greatest sources of inspiration, and friends Christopher Clayton, John and Aisha Wright, and Alana McClain for being his most ardent and influential supporters.

Table of Contents

List of Figures

Chapter 1
Introduction

Electromagnetic phenomena have and will always govern the world of men in discrete and insidious ways. Electromagnetic forces have demanded countless civilizations to witlessly marvel at their affects, but the work of history's most prominent electrical practitioners discovered how to make those same forces actually work for the progression of mankind. The pioneers of electromagnetic studies realized electricity and magnetism do not act independently of each other, but instead they exist in a dichotomous relationship. The realization allowed electromagnetism to become a relevant and influential academic pursuit. Instead of an ignorance born awe, electromagnetism is dumbfounding because it further highlights the forces that keep the precarious foundation of our universe in balance.

The father of electromagnetism, even though it had been heavily studied before him, Michael Faraday intrepidly pioneered the way for electromagnetism to be more than a subject of interest; he revolutionized its relevance in the fast changing world of the Romantic Era. While building upon the work of his predecessors Andre Ampere and Hans Oersted, Faraday became the first in recorded history to produce an electric current that resulted from a time varying magnetic field. Although the unit for capacitance is named for him, his experiment created the first controlled occurrence of electromagnetic induction [1].

From electromagnetic induction, Faraday used iron filings and the "lines of force" that surround magnets to gain a better understanding of how electric currents are influenced by magnets and, subsequently, where electromagnetic fields are conjured. That discovery paved the way for physicist James Clerk Maxwell to study the effects of electromagnetic radiation [2]. With this knowledge he derived that electromagnetic fields can exist independently of the presence of matter [3] and that electromagnetic waves are able to propagate through space [4]. Maxwell formulated four powerful equations that prove time varying electric and magnetic fields move through air at the speed of light that today are eponymously named Maxwell's equations:

$$\nabla \cdot \epsilon \mathbf{E} = \rho v \tag{1.1}$$

$$\nabla \cdot \mathbf{B} = 0 \tag{1.2}$$

$$\nabla \times \mathbf{E} = -\frac{\partial}{\partial t}\mu \mathbf{H} \tag{1.3}$$

$$\nabla \times \mathbf{H} = \sigma \mathbf{E} + \frac{\partial}{\partial t}\epsilon \mathbf{E} \tag{1.4}$$

Together, these equations are the most general descriptions of electromagnetic wave propagation [5].

Notice $\sigma, \mu,$ and ϵ in the representations of Maxwell's Equations above. They are of particular interest to the concentration because of their importance in describing wave behavior at the boundary between two media and the behavior inside any single medium. Knowing the constitutive parameters conductivity ($\sigma\ S/m$), electric permittivity ($\epsilon\ F/m$), and magnetic permeability ($\mu\ H/m$) allows for other significant information to be defined. Two essential quantities that are derived from those parameters are wave impedance (1.5) and the index of refraction (1.6) [5].

$$\eta = \sqrt{\mu/\epsilon} \tag{1.5}$$

$$n = \sqrt{\mu\epsilon} \tag{1.6}$$

Equations (1.5) and (1.6) can be manipulated to produce astounding results that have

been studied and tested enough to expand the study of classical electromagnetism into a

realm that not only distorts the conventional behavior of electromagnetic radiation, but it

completely upends the most basic competencies of the field.

Chapter 2
Metamaterials

In 1968 the Russian physicist Vincent Veselago conjectured a radical hypothesis that addressed the manipulation of the permittivity and permeability material quantities. Mathematically, he derived what would happen to an electromagnetic wave's propagation through a medium in which those manipulations have occurred. He approached his hypothesis by looking at the dispersion equation in the instance of an isotropic substance, which yields equation (2.1) [6].

$$k^2 = (\frac{\omega^2}{c^2})n^2 \tag{2.1}$$

Recall (1.6) above and square the index of refraction.

$$n^2 = \mu\epsilon \tag{2.2}$$

What if both the permittivity and permeability were to simultaneously become negative values while being evaluated as real numbers without the effects of material loss? The math regarding the index of refraction and dispersion equations would not diverge from their present form, but Veselago suggested three possible physical phenomena that could result.

The first suggestion is that nothing about the wave's propagation would actually change, that changing the signs of the permittivity and permeability would have no affect on a substance's material characteristics. The second is that converting these values to negative counterparts would violate nature and would be a perversion that could not exist.

Lastly, and with eventual and overwhelming evidence to support it, his third interpretation of the results suggested changing a substance's permittivity and permeability to negative values will fundamentally change the substance itself by giving it properties unique from its conventional characteristics [6].

With no such materials in existence, Veselago continued to carry out his research mathematically and investigated the Poynting Vector given in (2.3).

$$S = \frac{c}{4\pi} [EH] \tag{2.3}$$

In the dispersion equation, vector **k** is directed along the same axis as the phase velocity, while the energy flow described by the Poynting Vector is in the direction of the group velocity. In right handed materials, denoted by Veselago to be substances where both μ and ϵ are positive, the group and phase velocities will move in the same direction. In the case of a left-handed (or double negative) substance, both μ and ϵ are negative, the phase velocity moves 180° to the flow of power in the group velocity [5], also called the reverse Doppler Effect. Figure 2.1 below depicts anti-parallel phase velocity behavior.
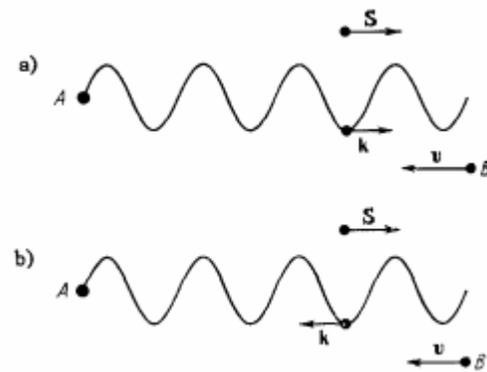
Fig 2.1. a) Phase and group velocity propagation in right-handed media. B) Anti-parallel movement of group velocity to phase velocity in left-handed media [6].

Further investigation led Veselago to take a look at electromagnetic boundary conditions. The four boundary condition equations below must be satisfied without regard to right-handed or left-handed media [6].

$$E_{t_1} = E_{t_2} \tag{2.4}$$

$$H_{t_1} = H_{t_2} \tag{2.5}$$

$$\varepsilon_1 E_{n_1} = \varepsilon_2 E_{n_2} \tag{2.6}$$

$$\mu_1 H_{n_1} = \mu_2 H_{n_2} \tag{2.7}$$

Veselago surmised, by inspection of the stated equations, that the vectors **i** and **j** in the wave's propagation would adhere to their initial direction of propagation no matter the material's positive or negative constitutive parameters, but the vector **k** would be reflected in a double negative substance environment. What this leads to is the case of a wave that propagates from a right-handed medium into a left-handed one. Instead of the wave's energy being reflected back into the right-handed medium, the wave will experience refraction at the boundary of the two media [6].

6

Reverse Cherenkov radiation is another one of the effects that was described by Veselago in 1968. Cherenkov radiation occurs when charged particles move through a medium at a speed that is greater than the phase velocity of light [7]. For Cherenkov radiation in a double negative material, the charged particle's velocity vector and its Poynting vector will move orthogonally to each other while the direction of wave propagation and radiation are anti-parallel [6].

Applications of Metamaterials

Beyond descriptions of the reverse Doppler Effect, reverse Cherenkov radiation and complete electromagnetic wave refraction at a boundary between right-handed and double negative media, there have been more interesting realizations and applications to come out of this topic that are just as preternaturally astounding. Because left-handed substances are not found in nature and were not made available at the time, Veselago's initial speculations at double negative materials went unanswered for nearly thirty years. It was not until physicists like Sir John Pendry at the Imperial College in London and Dr. David Smith at Duke University at the end of the 20th century did the research progress [5]. Their work has led to the designation of this field of work as metamaterials.

The prefix "meta" comes from the Greek language and in this instance it means beyond, as in a material that is beyond its time. The terms metamaterials, double negative, left-handed, and negative refractive index materials are all used to indicate materials with negative permittivity and permeability values.

Metamaterials research over the last decade has grown drastically. So much so, that the potential of using them in everyday life has morphed out of the regime of science fiction and into reality. The applications of metamaterials include super lensing, antennas,

acoustics, seismic activity protection, EM radiation absorption, and, the paramount of all field-related research, cloaking. Selected applications mentioned above are described below.

Veselago proposed that convex and concave lenses' properties are transposed in the case of negative refracting lenses, meaning that the concave lens has a converging effect and the convex lens is divergent. Figure 2.2 below depicts the phenomenon [6].
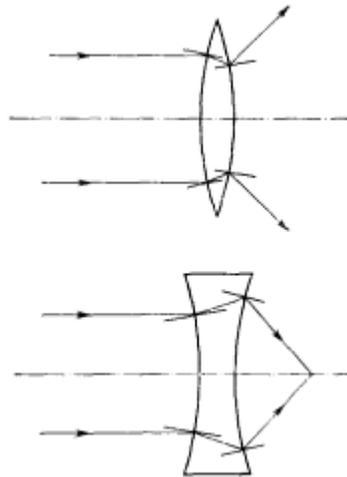

Figure 2.2. A divergent convex lens (top) and a convergent concave lens (bottom) made of metamaterials [6].

The equation given in (2.8) relates the lens's radius of curvature in the numerator and its index of refraction in the denominator to its focal length.

$$f = \frac{R}{(n-1)} \qquad (2.8)$$

Equation (2.8) shows that the index of refraction, n, gives the focal length distinct values at either positive or negative index of refraction values. Right-handed lenses do not refract EM fields, but left-handed lenses can. Because of this feature, double negative lenses have benefits that include compact design in small electronic applications and near field electromagnetic ray amplification [8].

Metamaterial based antennas can be broken down into two regimes: leaky-wave antennas and resonator-type small antennas. Leaky wave antennas derived from metamaterials structures have the added benefit of backward to forward beam scanning, including the broadside radiation. For small resonator antennas, size and efficiency are the trade-offs engineers have to contend with. One of the benefits metamaterials proposes to these antennas is allowing for a smaller size while maintaining the integrity of the antenna's radiating abilities [9]. Antennas that implement double negative features can radiate power without the loss incurred from reflected energy that is usually observed in right-handed antennas.

To give an example of metamaterial antennas, a team at China Jiliang University in Hangzhou, China successfully designed a compact patch antenna that was based on complimentary split ring resonators. This special type of ring resonator will be explained in greater details in the pages to follow. The team used a microstrip patch because of its relatively easy design, size, and low cost. The metamaterial components boosted the antenna's gain, directionality, and lowered the return loss at the frequency of interest [10].

Metamaterials research has even been extended beyond the electromagnetics regime. Mechanical waves, like electromagnetic waves, can be significantly altered when they propagate in the presence of metamaterials. They can force negative values upon the mechanical parameters of compressibility and mass density [11], just as they are capable of doing to the permittivity and permeability in electromagnetic applications. Acoustic metamaterials is the name given to those double negative structures that affect the behavior of mechanical waves that operate in the form of sound.

Researchers in [12] used acoustic metamaterials alongside microelectromechanical systems (MEMS) technology. MEMS vibrational gyroscopes are desirable because of their low cost, low power consumption, and small size compared to traditional to gyroscopes, but they are a lot more sensitive and susceptible to ambient noises. To mitigate this issue in [12], an inertial acoustic metamaterial made from a one-dimensional array of Helmholtz resonators were employed to achieve sound attenuation at a desired resonance frequency of 14.5 kHz. The acoustic metamaterials lowered the noise by 34 dB while a control box composed of traditional sound attenuation devices only lowered the sound by 16 dB.

Super lensing, antennas, acoustics and many other applications are highly valuable and worthwhile topics in the metamaterials field, but the greatest potential achievement in metamaterials research is electromagnetic cloaking. The frequencies of particular interest are those in the visible light spectrum. A "cloak" conceived with metamaterial structures can be used to cover an object which will lead to the refraction of planar waves around the object with little scattering. There are numerous methods that have been researched, but there are two that have consistently yielded favorable results. The first is the scattering cancellation technique, which diminishes the scattering of an object by surrounding it with layers of a dielectric that has a permittivity value that is less than one. Coordinate transformation is another effective technique. It creates a volume in space that does not allow the EM fields to exist but maneuvers them around the object covered by some lossless metamaterial device [13]. Researchers at Duke University demonstrated coordinate transformation using a copper cylinder at microwave frequencies. Figure 2.3 shows the field patterns that resulted from the experiment [14].
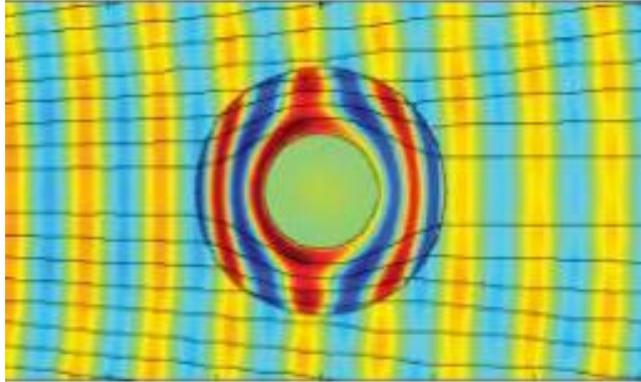
Figure 2.3. The black lines show the flow of power while the red, yellow, and blue show the microwaves as they move over the shrouded object. The cloak is in the inner radius of the object, causing the microwaves and power to refract around its center [14].

Translating this experiment to frequencies along the visible spectrum is much more difficult because researchers have only been able to produce these results using very narrow bandwidths, whereas the bandwidth for one color on the visible is relatively large when considering metamaterial applications. The reasons for that are directly related to how metamaterial devices are actually constructed.

How They Are Made

JB Pendry drew parallels between the characteristic properties of metamaterials and materials that occur naturally. He explained that those substances found in nature derive their properties from their miniscule atomic and chemical compositions. In the case of metamaterials, their properties are a product of the sub wavelength sizes of man-made structures. Metamaterials are designed at wavelengths much less than those at their frequency of operation, which can be from the lower GHz range up to THz, and can control the near field which is highly sensitive to the permittivity and permeability of microstructures and nanostructures. There are two types of structures that are used to develop metamaterials: resonant elements and intersecting straight wires. Pendry focused

11

his works on resonant elements [15]. Figure 2.4 shows a conceptual comparison of natural materials to metamaterials and the type of resonant structure that could create a metamaterial object.
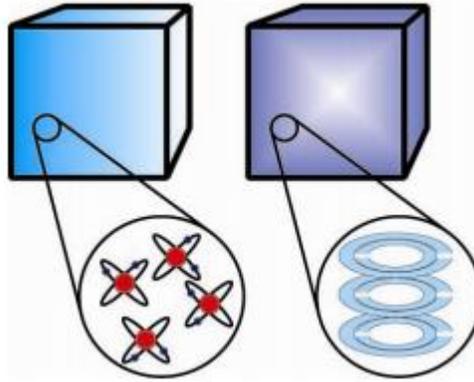

Figure 2.4. A conceptual comparison of natural material composition to that of metamaterials. The figure to the right shows the resonant structure studied by Pendry [15].

Split Ring and Complementary Split Ring Resonators

The resonant structure Pendry conceived is called a split ring resonator (SRR). A negative effective permeability, μ_{eff}, is induced in the SRR when it operates at its resonant frequency. A current induced in the rings due the presence of a magnetic field will become a strong displacement current when it flows from one ring to another across the space between them [16]. The circuit diagram in Figure 2.5 is used to determine the resonance frequency of a SRR loaded transmission line [17] and an array of split ring resonators is depicted in Figure 2.6 [15].
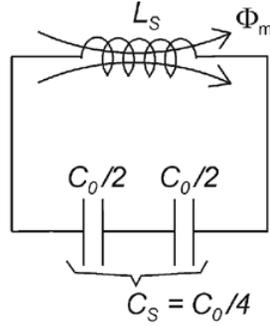
Figure 2.5. The equivalent circuit model used in the determination of the split ring resonator's frequency response on a transmission line. C_0 is the capacitance between the inner and outer rings. The equation for that capacitance is $C_0 = 2\pi r_0 C_{pul}$. C_{pul} is the capacitance/length between the rings. f_0 is the resonance frequency and it is equivalent to $(L_s C_s)^{-1/2}/2\pi$. C_s is $C_0/4$ and it is the series capacitance of the SRR's top and bottom halves. r_0 is the radial distance from the ring's center to the outer edge of the inner ring. L_s is seen as the inductance of one ring with a radius r_0 and a width equal to that of the rings' [17].
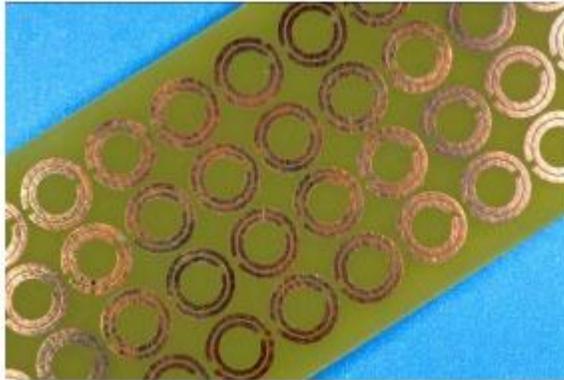

Figure 2.6. An array of copper etched split ring resonators on a printed circuit board [15].

The outer split of the split ring resonator is there because it allows it to have a resonance at wavelengths greater than the ring's diameter. The inner ring's split and opposite orientation to the outer ring's split is there to incite capacitance in the gap region within the SRR. Its function is to decrease the structure's resonant frequency and to contain the generated electric field. Equation (2.9) was derived by Pendry to calculate the effective permeability of the SRR after a magnetic field acts upon the structure [18].

$$\mu_{\text{eff}} = 1 - \frac{\pi r^2/a^2}{1 - 3\ell/\pi^2\mu_0\omega^2 Cr^3 + i(2\ell\rho/\omega r \mu_0)}$$

$$= 1 - \frac{F\omega^2}{\omega^2 - \omega_0^2 + i\omega\Gamma}.$$

(2.9)

In (2.9), ρ is resistivity around the outer ring's circumference, ω is the incident field's frequency, ℓ is the layer difference, a is the lattice parameter, r, is the radial distance from the ring's center to the inner edge of the inner ring, F is the area of the SRR within a unit cell, Γ is the dissipation factor, and C is the capacitance between the inner and outer rings [18].

In general there are two types of split ring resonator configurations that are more familiar than other types in the research community: broadside-coupled and edge-coupled split ring resonators shown in Figure 2.7 [19].
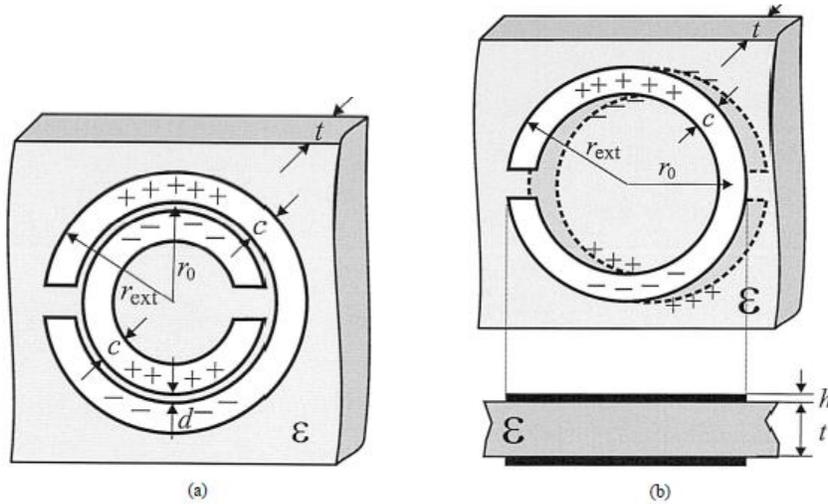

Figure 2.7. a.) Edge-coupled split ring resonator. b.) Broadside-coupled split ring resonator with a layered view attached [19].

The edge-coupled design was first conceived by Pendry. Because it does have instances where cross-polarization is an issue, the broadside-coupled structure was designed. Another advantage of the broadside-coupled SRR is isotropy within its plane and a

possibly smaller electric size [19], but the edge coupled SRR is still more relevant because of the stronger knowledge base available on it.

The split ring resonator is not the only resonant structure capable of realizing a metamaterial device. Its complement structure, called a complementary split ring resonator (CSRR), has also become a factor in the conversation of metamaterial transmission lines.

The SRR is etched onto a dielectric substrate; the CSRR is etched coplanar into a metalized layer, usually the ground plane or signal line depending on the line's size. Also, whereas the SRR is excited by a propagating magnetic field, the CSRR responds to an electric field that travels parallel to the ring's axis. The CSRR will attain a negative permittivity at its resonance [16], which is opposite to the SRR's negative permeability at resonance. The circuit diagram in Figure 2.8 is that of a CSRR loaded transmission line and Figure 2.9 shows a set of complementary split ring resonators etched into a metal layer [17].
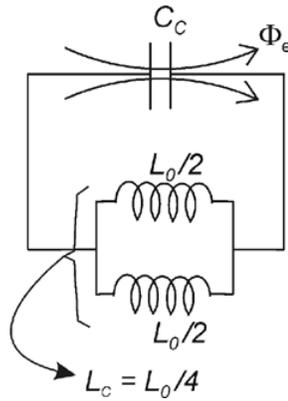
Figure 2.8. Equivalent CSRR circuit diagram used to determine frequency response [15]. C_c is the capacitance that results from a disk radius of $r_0 - c/2$ inside a ground plane with a distance c between the disk's edge and the inner edge of the ground plane. r_0 and c are the same as the SRR model's, just inverted. $L_0 = 2\pi r_0 L_{pul}$ and L_{pul} is the inductance/length of the coplanar waveguide connecting the inner disk of the CSRR to the larger ground area [17].
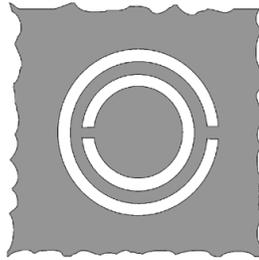

Figure 2.9. A coplanar CSRR etched into a metal ground layer [15]. The CSRR is the complement of the SRR is every way when losses are not accounted for, even the resonance frequency value [17].

Chapter 3
Filters Constructed from Metamaterial Structures

As stated before, the SRR and CSRR are each capable of realizing negative values for only one of the constitutive parameters that determines a material's right-handed or left-handed properties. To reiterate, the SRR will have a negative permeability at its resonance frequency and the CSRR will have a negative permittivity at the same resonance. How can a true metamaterial structure be realized when only one of the two parameters is reversed? This thesis will explore that topic with the use of a CSRR loaded transmission line bandpass filter.

Types of Metamaterial Filters

Composite right/left-handed (CRLH) transmission lines is the term generally used to describe a transmission line that is the result of metamaterial structures. The first attempt at the special types of filters was seen in 2002 with the use of series capacitances and shunt inductances. Capacitive gaps and induction as a result of metal loading on specific areas of the signal line gave rise to left-handed propagation at certain frequencies. Then at higher frequencies, the capacitance and inductance will switch loading types. The capacitance becomes shunt impedance while the inductance becomes series impedance and brings forth the composite right/left-handed behavior that classifies the filter as a metamaterial device [20].

In 2003 a CRLH transmission line was constructed with a coplanar waveguide design that used split ring resonators. They were placed on the bottom of the substrate beneath the ground pads attached to the top of the substrate. The SRRs and signal layer allowed the transmission line to have left-handed propagation at lower frequencies and right-hand propagation at the higher end of the spectrum. Figure 3.1 shows the transmission line's circuit model [20].
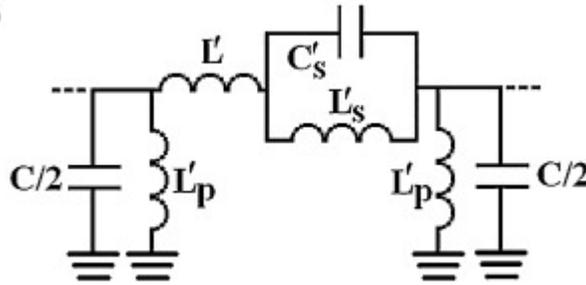

Figure 3.1. An equivalent circuit diagram of the SRR loaded composite right/left-handed coplanar waveguide. L_p is the inductance between the signal and ground lines, L is the line inductance, L_s and C_s are the inductive and capacitive tank circuits, and C is the line capacitance [20].

Split ring resonators were the more popular choice for metamaterial filters until the complementary split ring resonator was conceived. The CSRR loaded transmission line uses capacitive gaps in the signal line on a microstrip configuration in the CSRR filter's most widely used form. The complementary split ring resonators implemented in the design are of course etched in the ground plane of the transmission line and are placed directly below the signal line's capacitive gaps. Figure 3.2 depicts the CSRR and signal line/gap combination. Figure 3.3 is the circuit model [20].

Figure 3.2. A until cell representation of a CSRR loaded transmission line filter with a complementary split ring resonator etched below the capacitive gap in the signal line [20].
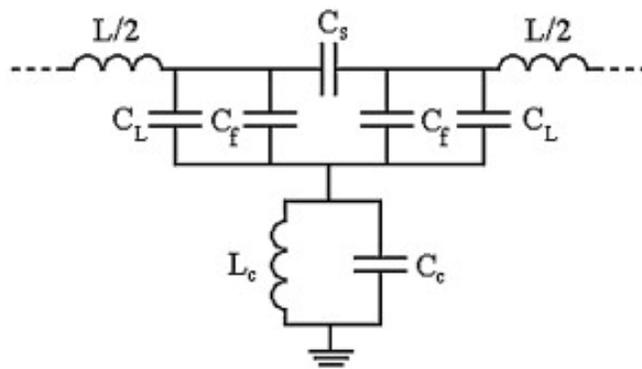

Figure 3.3. The equivalent circuit model of a CSRR loaded transmission line with signal layer capacitive gaps. L is the signal line inductance, L_c and C_c are the tank circuit representation of the CSRR, C_s is the series capacitance of the line gap, C_f is the fringing capacitance of the line gap, and C_L is the necessary coupling between the signal and the CSRR [20].

The three types of filters discussed above are the most basic structures of metamaterial transmission line filters. More filter types have been derived and constructed based on the SRR and CSRR filters. One example is ultra-wide bandpass filters that are based on the complementary split ring resonator filter design [20]. The greatest advantages to metamaterial filters are their compact size and controllability.

CSRR Metamaterial High Pass, Bandpass, and Stop Band Filter Design

Ambitious designers consistently attempt to realize filters that are simultaneously high performing, cheap, designed with a low insertion loss, and compact. Because of the progress of wireless technology and ever decreasing feature sizes, wide-band bandpass filters that fit the criteria previously mentioned have become an increasingly obvious necessity. There are several designs with the priority of addressing the filter's bandwidth, but that unsuccessfully mitigate the other cost and performance issues. Fortunately, a bandpass filter using complementary split ring resonators can deliver the bandwidth, size, cost, loss, and performance needed to propel the work and research of the communications field into the future.

In [21], it is discussed that using a metamaterial transmission line that implements complementary split ring resonators can produce both low pass and high pass filters. It is a combination of both that will bring about a bandpass filter. Simply adjusting certain parts of the CSRR transmission line design will influence and ultimately alter the structure's frequency response.

The high pass filtering capabilities of the transmission lines are affected by the areas surrounding the capacitive gaps in the signal line. Increasing the metal areas just before the gap increases the capacitance seen by the propagating signal. [21] discusses several patterns, including rounded parallel, elongated parallel, and jagged ends. Examples of those patterns are shown in Figure 3.4.
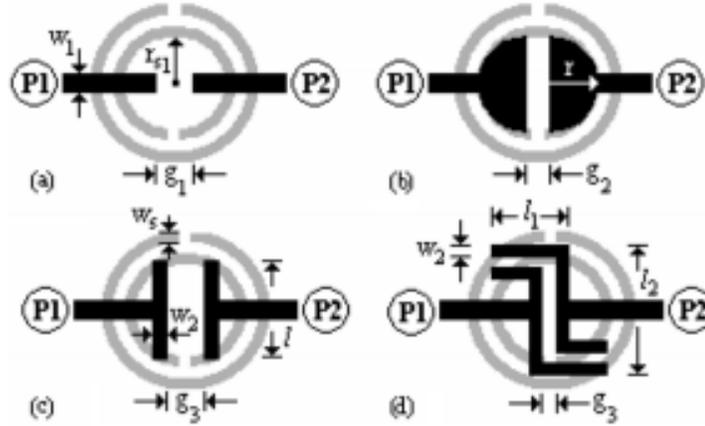
Figure 3.4. Potential configurations for high pass filter designs in a CSRR loaded transmission line. a.) Regular capacitive gap. b.) rounded capacitive gap. c.) elongated parallel capacitive gap. d.) jagged parallel capacitive gaps [21].

The low pass filtering is determined in a way that is similar to that of high pass filtering. In [21], a U-shaped structure, two shunts coming off of the signal line directly above a ground-etched CSRR that precedes the capacitive gap of the high pass filter section, was designed to produce the low pass filter component. Coupling by the U-shaped structure and the CSRR causes the low pass filter's cutoff frequency to be higher than the CSRR's resonance frequency, but lower than the shunt structure's cut off frequency. Figure 3.5 shows the low pass and high pass components of the cascaded bandpass filter design.
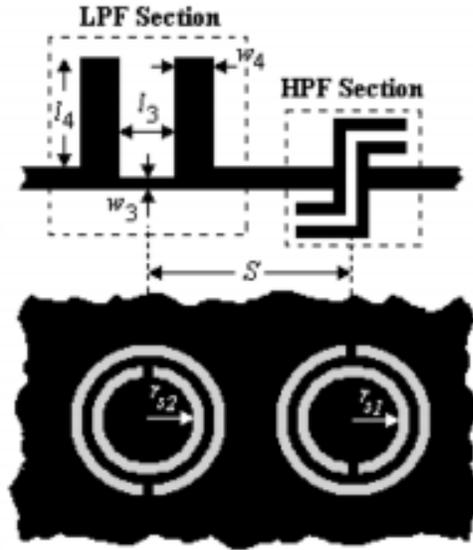
Figure 3.5. A depiction of the high pass and low pass filtering sections of the CSRR loaded transmission line [21].

In [22] a stopband filter was developed using complementary split ring resonators. Kshetrimayum et. al. found that by simply etching CSRRs into the ground plane of a microstip transmission line, a narrowband stop band filter could be produced. Unlike the low pass, high pass, and bandpass filters mentioned above, there was no need for a more complicated design of the signal line. A line of uninterrupted metal produced a stop band filter.

Flexible Bandpass, Stopband, and High Pass Filter Design

Expounding on what was done in [23]; this thesis will discuss a bandpass, stopband, and high pass filters made with a single-ended CSRR loaded transmission line. These filters' low pass and high pass filtering components are slightly different from the ones presented in the discussion above. These filters were also designed with flexibility in mind. The interest in this comes from attempts to realize a cloaking structure that is

22

compatible with any shape [23]. Designing any kind of practical filter that is capable of doing that is a step in the right direction to further progress metamaterials research.

For this thesis, the structures were not fabricated and physically tested. Instead, the filters were evaluated with a series of simulations in Ansys's High Frequency Structure Simulator (HFSS). HFSS allowed for the filters to not only be simulated as planar structures, but it was also useful in evaluating the filters at different radii of curvature in order to compare the curved structures' consistency and compatibility to the planar cases. Specifics of the filters' designs will be given in a latter section of this thesis, but a brief explanation of HFSS immediately follows this chapter.

Chapter 4
HFSS

Ansys's electromagnetic computer modeling software, HFSS, has become an industry standard. Its user friendly graphical user's interface is intuitive enough to help even the most novice RF, microwave, and electromagnetic engineers create anything that starts in the deepest recesses of their imaginations. The software opens up and gives its user free reign to draw, scale, and measure whatever his heart and needs dictate. Once designed, the software offers a myriad of simulation options; ranging from power based solutions to incident wave modeling. Then the simulations can be conducted thoroughly or quickly and with as much data across as many frequencies as warranted. Once all of the data has been generated, HFSS allows the user to process and analyze it in any way that satisfies its user's requirements. HFSS is an extremely versatile software package that has played no small part in assisting the world's engineers and scientists to advance the field of electromagnetism.

How It Works

Ansys designed HFSS to use the Finite Element Method (FEM) for solving complex microwave structures. This method will divide a structure into smaller pieces and define a "finite element." HFSS breaks objects down into many tetrahedrons and the combination of the separate tetrahedrons is called a mesh. Each individual tetrahedral is

solved using Maxwell's equations while keeping each piece connected at its boundaries. A field solution is obtained for the entire structure by constructing the solutions from each piece. Once the field solution has been obtained for the entire form, an S-parameter matrix is generated. Because Maxwell's equations are the basis of the simulator, HFSS does not solve objects by using electric circuit parameters like voltages and currents; instead it uses electric and magnetic fields. These fields must be able to exist within the evaluated structures in order for HFSS to work properly [24].

What Makes It Work

HFSS does not just spit out information after a user presses "run," it forms a mesh and iteratively constructs and refines it, particularly in the areas where the fields are most complicated, to ensure it is computing the correct results. This process of redefining and updating meshes to approach the most correct solution is called an adaptive solution [24]. The user can determine how much room for error will be allowed in the HFSS solution by defining the program's adaptive sweep settings.

Before HFSS begins to adaptively solve anything and after the user creates the model, the kind of solution the solver should work toward, the boundaries, and the excitations all have to be set. There are three solution types available in HFSS: driven modal, driven terminal, and eigenmode. The driven modal solution is the most common and is used when evaluating simple transmission line, microstrip, and waveguide structures. It presents its data in a conventional S-matrix. Driven terminal is similar to driven modal, but it is mainly used to solve transmission lines with multiple signals for Signal Integrity (SI) purposes. It also presents an S-matrix, but it is based on voltages and

currents. The last solution type is the eigenmode solution. It provides a detailed report on the resonances in a structure and the fields at those resonant points [24].

Boundaries in HFSS are used to either create an electromagnetic model or to simplify and contain a geometric model. There are twelve boundary options to choose from, depending on the needs of the user. The most relevant one to this thesis is the Radiation boundary. This boundary type will create an open model and is applied to the outer surfaces of the user-defined area which is a quarter of a wavelength away from the simulated model. The radiation boundary is intended to set a point at which waves that will radiate to infinity will be truncated in order to keep the simulation as simple as possible [24].

There are seven excitation options in HFSS and they allow the user to indicate field, voltage, charge, and/or current sources to drive the simulation. Only two will be presented here. The wave port excitation is one of the most commonly used with transmission lines and is used in this thesis. It provides S, Y, and Z parameters and will also relay port impedance information. Because the wave port is seen as a waveguide when energy enters it, the port's size is an important consideration to take into account. The floquet port was also considered for the simulation central to this thesis. It is employed when simulating planar and periodic structures, but more specifically, it is more relevant in spatial situations and is less appropriate for simulating a microstrip filter [24].

Drawing a structure, initializing "simulation rules," and determining how something should be solved are all it takes to use the electromagnetic solving capabilities of HFSS. The rendered solution can be as exact or approximate as the user wishes. The

exact options and choices that were made concerning this thesis topic will be discussed as the project is presented.

Chapter 5
Filter Design

The three microstrip transmission line filters evaluated in this thesis-pass band, high pass, and stop band- are all designed with the same substrate and ground plane configurations and they are based on the features and sizes detailed in Jonathan Richard's master's thesis work [23]. The most significant difference in each design is attributed to the signal layer, which has different designs to achieve each of the three desired filtering affects.

Copper Metal

Copper is the metal chosen for each of the filters' metal layers. This includes the signal and ground layers. Copper has a relative magnetic permeability of approximately 0.99 H/m and electric permittivity of 1 F/m. Its conductivity is $5.8x10^7$ S/m. Other than being an extremely reliable and sufficient conductor, copper was chosen because of its ubiquitous use and malleability, which will be necessary for curved metamaterial filtering structures that are practical in real-world applications.

The Ground Layer

The ground's dimensions are 4 mm in width, 18 μm in thickness, and 10.5 mm in length. Complementary split ring resonators are etched coplanar to the ground plane and are spaced evenly, 0.57 mm a part, throughout the length of the ground plane. The rings'

dimensions are based on the resonance frequency that is desired to be achieved. Recall, each CSRR consists of an inner and outer ring. The inner ring has a diameter of 1 mm measured from one inside edge to the other. The actual ring "air" gap is 40 μm. The distance between the inner ring and the outer ring is 135 μm. The outer ring has an inner edge to inner edge diameter of 1.35 mm. Its "air" gap is the same as the inner ring. The metal gap that keeps the rings open and unable to complete the circle is 300 μm. The entire ground plane is 10.5 mm long. These dimensions are slightly larger, by approximately 10 μm, than those seen in [23]. Equations in (5.1-5.4) can be used to calculate the frequency response. Figure 5.1 is an image of the CSRR-etched ground plane in constructed in HFSS.
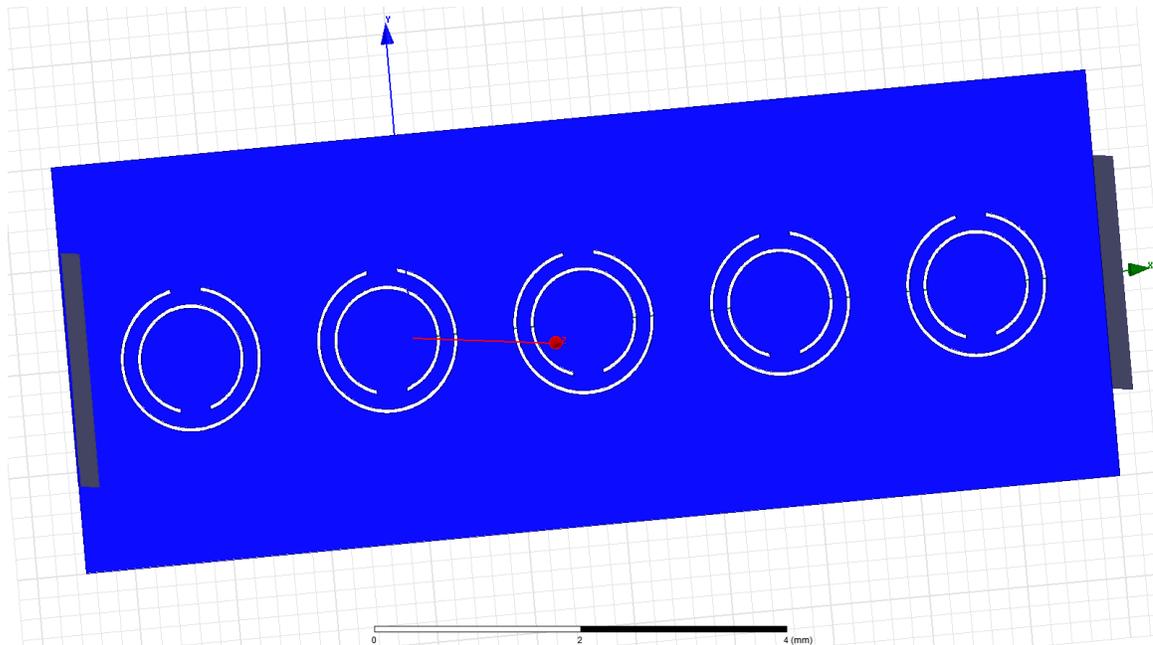
Figure 5.1. A depiction of the ground plane etched with complementary split ring resonators

How important the complementary split ring resonators are to the filters' designs cannot be overstated.

The Substrate Layer

Liquid Crystal Polymer (LCP) is the substrate implemented in the filters' designs [25]. LCP is a very unique polymer due to its composition of rigid yet flexible interlocking monomers that will align themselves along the path of shear flow during fabrication processes. Unlike other polymers that contain monomers that will sporadically rearrange, the monomers in LCP will retain their rigidity and path of alignment.

LCP has several chemical properties that make it a viable substrate to use in a metamaterial filter design. Its melting point, rigid structure, and surface roughness are all desired properties when integrating a copper signal trace to its design. More so than silicon substrates, LCP can introduce smaller trace sizes to a design while operating at very high temperatures [26]

The benefits of using LCP, as applied to the filters simulated here, are low loss and its ability to retain its dielectric constant at frequencies up to 40 GHz. In these designs, the LCP dielectric constant is 3.1 and has a dielectric loss tangent of approximately 0.004 [25]. Dimensions of the LCP substrate include a thickness of 4 mil, a length of 10.5 mm, and a width of 4 mm [23]. Figure 5.2 is a depiction of the LCP substrate layer in HFSS.
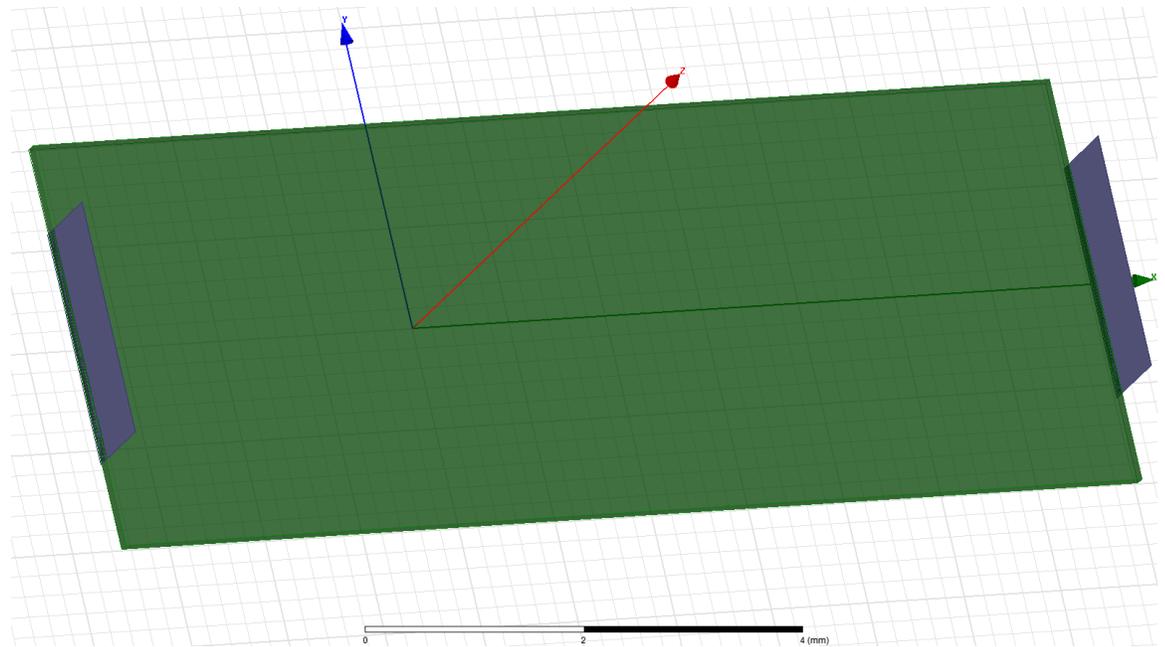
Figure 5.2. The LCP layer used in the various filter designs

The Signal Layer

A 50 Ω characteristic impedance was the design goal for the signal line. Based on

the heights and widths of the substrate and the metal thickness that would be used, the

signal line has a width of 232 um and is 10.5 mm long [23]. The most unique feature of

the signal layer is the different aesthetic forms. These features, along with the advent of

the complementary split ring resonators, had to be used in order to achieve the band stop,

high pass, and band pass filters.

The band stop filters have a simple design that is normally seen in transmission

line applications. The high pass filters were simulated using one of the designs mentioned

above; there are consistent and evenly spaced capacitive gaps in the signal line that are

adjacent to elongated metal lobes on either side of the gap. The band pass filters are

similar to the high pass filters, but the elongated signal junctions do not appear alongside

31

the capacitive gaps. Figure 5.3 shows the three types of signal lines used to develop the high frequency filters.
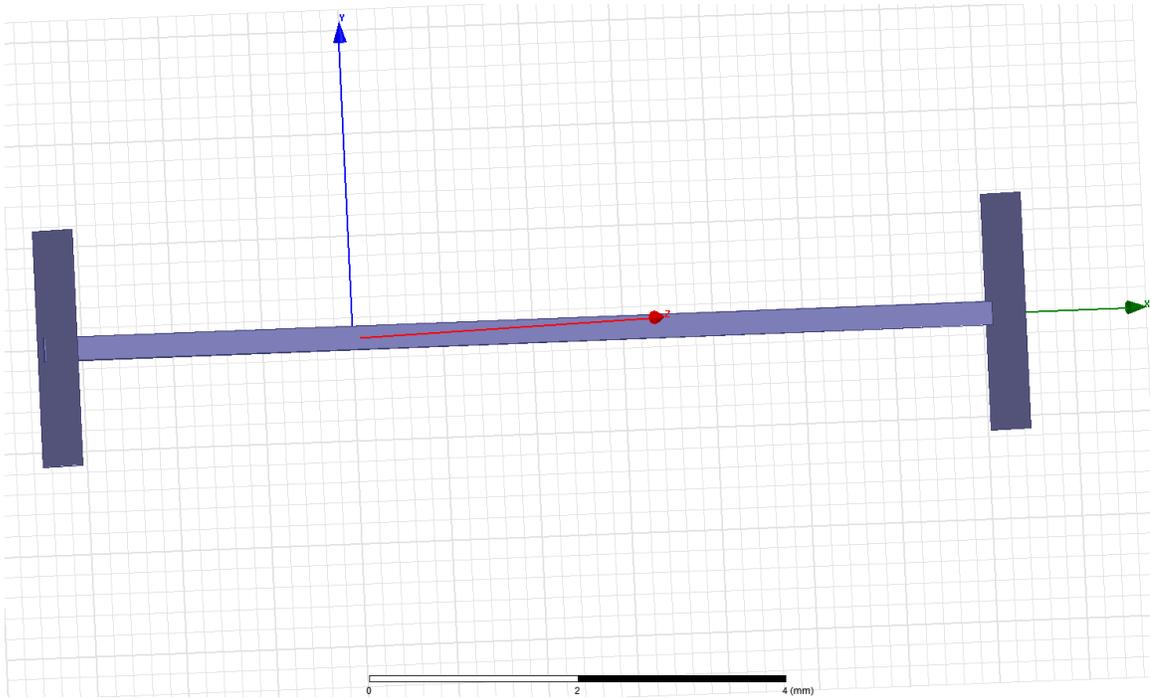
Figure 5.3a. The signal line design for the band stop filter
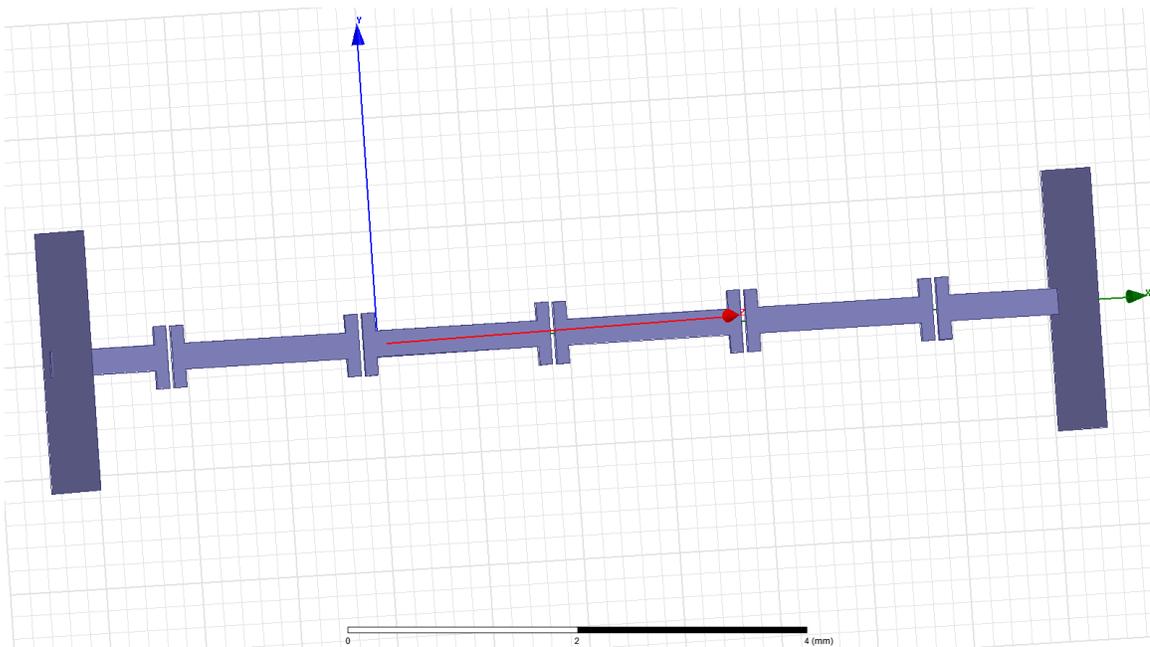
Figure 5.3b. The signal line design for the high pass filter.
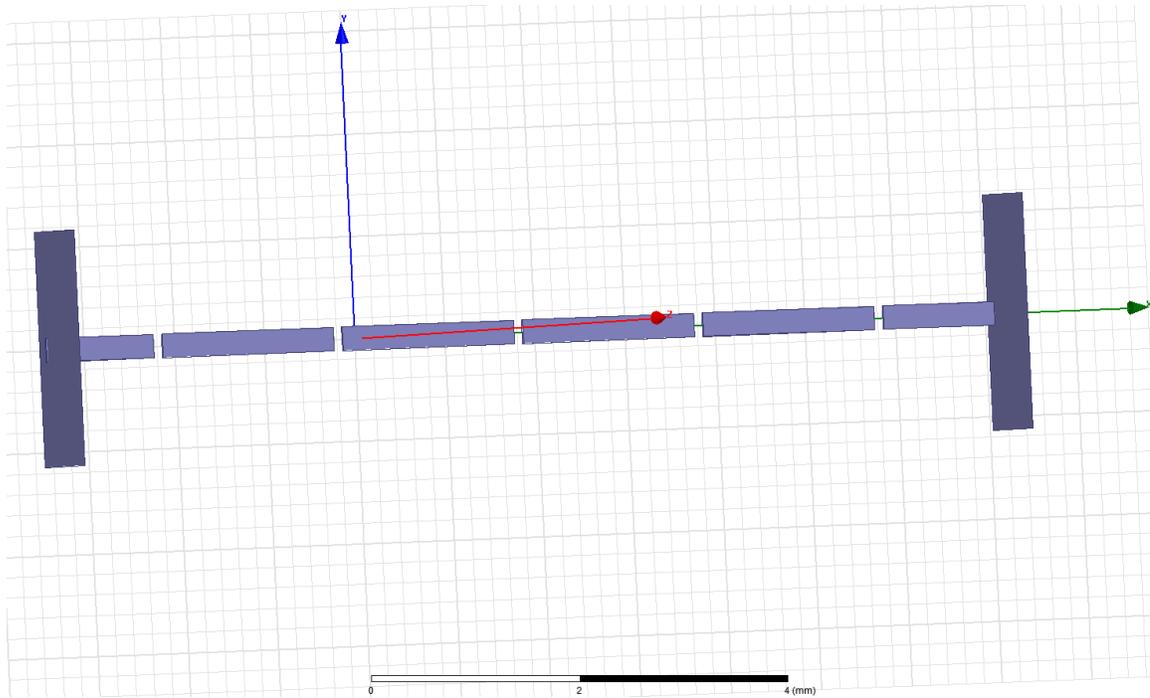
Figure 5.3c. The signal line design for the band pass filter

The design of the high order high frequency filters was conceived using the equations listed above and those seen below. The equations in (5.1) and (5.2) determined the resonance frequency of the CSRRs. What these equations show is an increase in the rings' radii will produce a lower resonance frequency and a wider metal gap in the rings will result in a higher resonance frequency. (5.3) can be used to calculate their effective permittivity [23]. Figures 2.8, 2.9 and 3.2 should be referred to. The structures resonate between 17.5 GHz and 22.5 GHz. Figure 5.4 shows the entire high pass filter structure.

$$f_H = \frac{1}{(2\pi\sqrt{L_c C_c})}$$

(5.1)

$$f_z = \frac{1}{(2\pi\sqrt{L_c(C + C_c)})}$$

(5.2)

$$\varepsilon_{eff} = \frac{C_R}{l} - \frac{1}{\omega^2 L_L l}$$

(5.3)
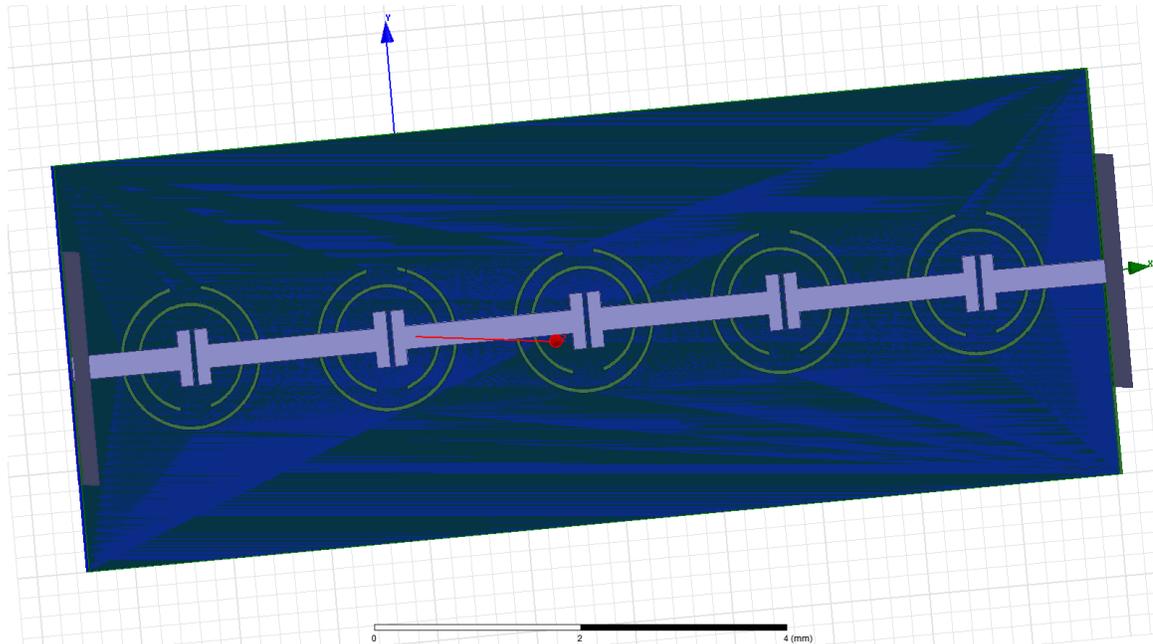
Figure 5.4. The complete (high pass) filter design.

The curved filters below that are compared to the planar filters consist of the same ground plane, substrate layer, and signal layer parameter specifications that are mentioned above. Of course, the only controlled difference between the two sets of filters, planar and curved, is the radius over which they are bent. To maintain a consistent signal length of approximately 10.5 mm and for simplicity regarding the simulation, the filters experience a radius of curvature of 3.3026 mm.

Implementing and configuring the simulation for these designs in HFSS was a much more cumbersome task for both the planar and curved structures. The next chapter will give more insight into the step-by-step process of crafting those constructions for simulation in HFSS.

Chapter 6
HFSS Construction

Building the filters in HFSS involved understanding the 3-D, and often complex,

geometric capabilities of the EM solver. Unlike most other software packages of its kind,

HFSS's graphical user interface uses actual 3-D drawings to realize its structures instead

of the planar approach to 3-D simulations like those seen in Agilent's Advanced Design

System. The most significant benefit of using 3-D drawings is greater creative license.

Users can manipulate these structures to construct almost any structure without the

limitations of planar lines on a page. On the other side, users will have to become very

creative with the geometry calculations and layered approaches used to actually make

highly curved, rounded, and dissected structures. What follows describes how the filters

were built.

Project Window

When a new project is opened in HFSS the user is given a blank canvas that

displays the x, y, and z axes. The most important toolbars at the top of the page are used

to draw and manipulate the views of the 3-D structure. The panel on the left side of the

screen provides relevant project information. These are all shown in the figures below.
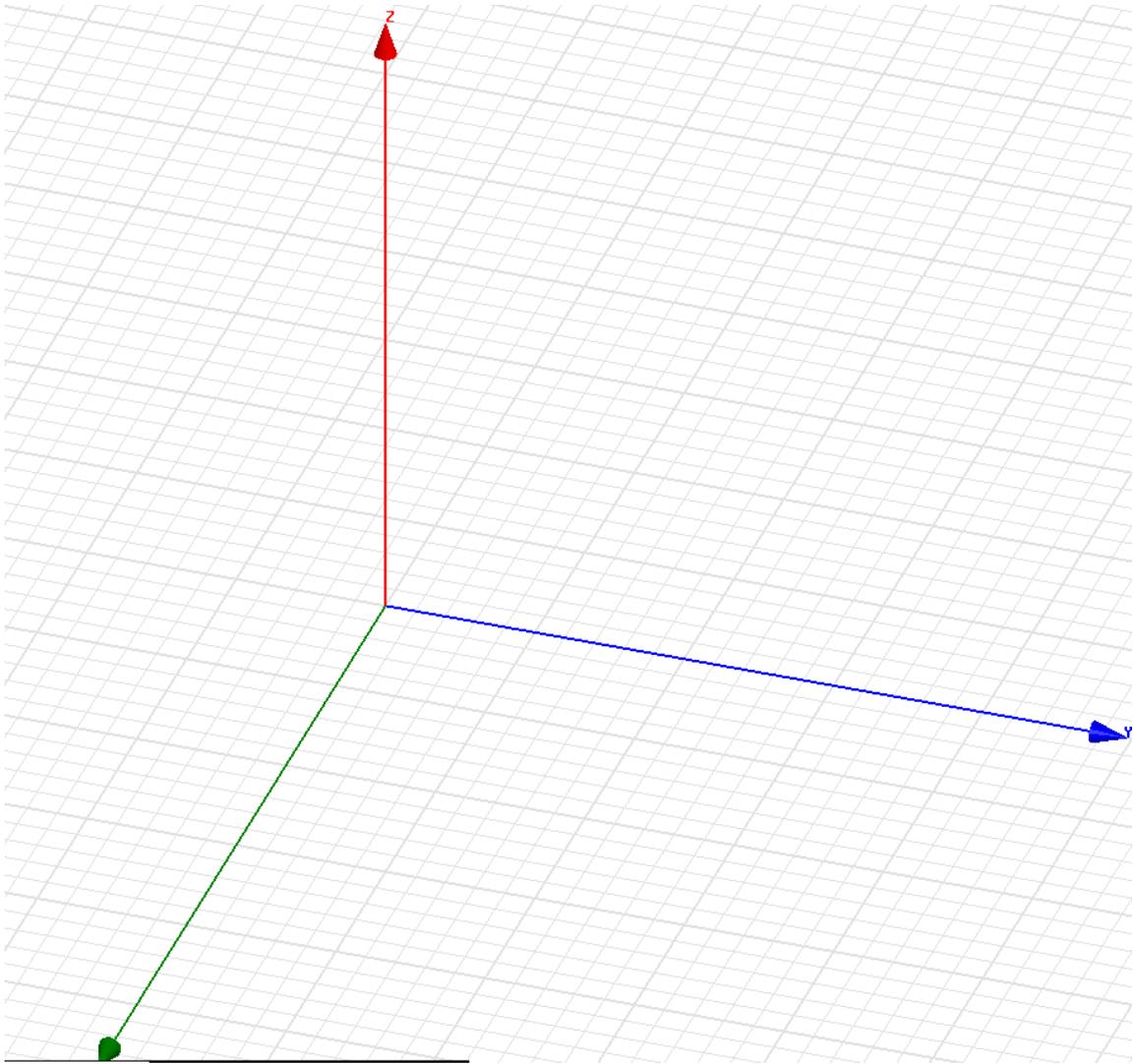
Figure 6.1. HFSS blank canvas screen seen during the initial stages of a project

Figure 6.2. These toolbars (rotated by an angle of 90 degrees) are used to design 3-D structures in HFSS. The images encircled are the primary tools used for drawing and manipulating the views of different structures.
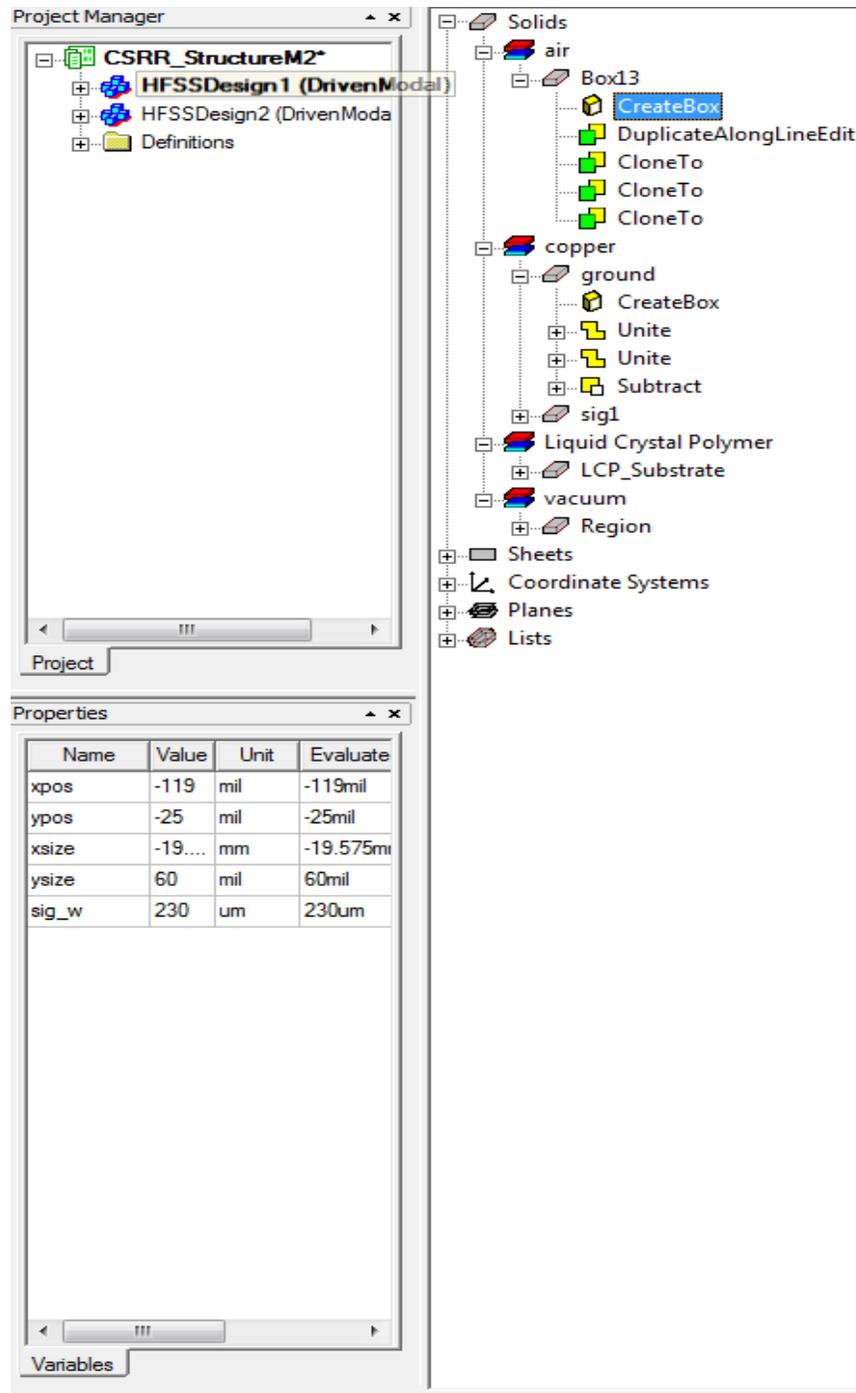
Figure 6.3. The Project Manager panel located on the left side of the screen which displays information about the project in progress.

Using HFSS to design a planar transmission typically involves stacking layers of cubic drawing structures highlighted in Figure 6.2 on top of each other. The most difficult part of this is keeping up with the dimensions and layer placements, which users will

have to define manually. Designing filters that have complementary split ring resonators

required many Boolean functions, particularly the subtraction and unite functions, to be

used habitually.

Constructing a Planar Design

To reiterate, the dimensions of the CSRR filter structures, the ground plane is 18

um thick and the substrate is 4 mil thick. Those measurements will place the signal layer

approximately 120 um above the bottom of the ground plane, which is along the z-axis.

The x and y axes positions are typically determined in a way that will lend similarity

across the origin to the structures. The width, 230 um measured along the y-axis, begins

at -115 um and the length, approximately 10.5 mm measured along the x-axis, will begin

at -5.25 mm. The width and length grow in the positive direction so they are initialized on

the negative side of the axes. An example of part placement parameters is show in Figure

6.4.

Properties: CSRR Structure - HFSSDesign1 - Modeler

Command

Name	Value	Unit	Evaluated Value	Description
Command	CreateBox			
Coordinate Sys...	Global			
Position	-5.25mm ,-0.115 mm, 0.1196 mm	mm	-5.25mm , -0.11...	
XSize	-10.525	mm	-10.525mm	
YSize	sig_w		230um	
ZSize	18	um	18um	

☐ Show Hidden

OK   Cancel
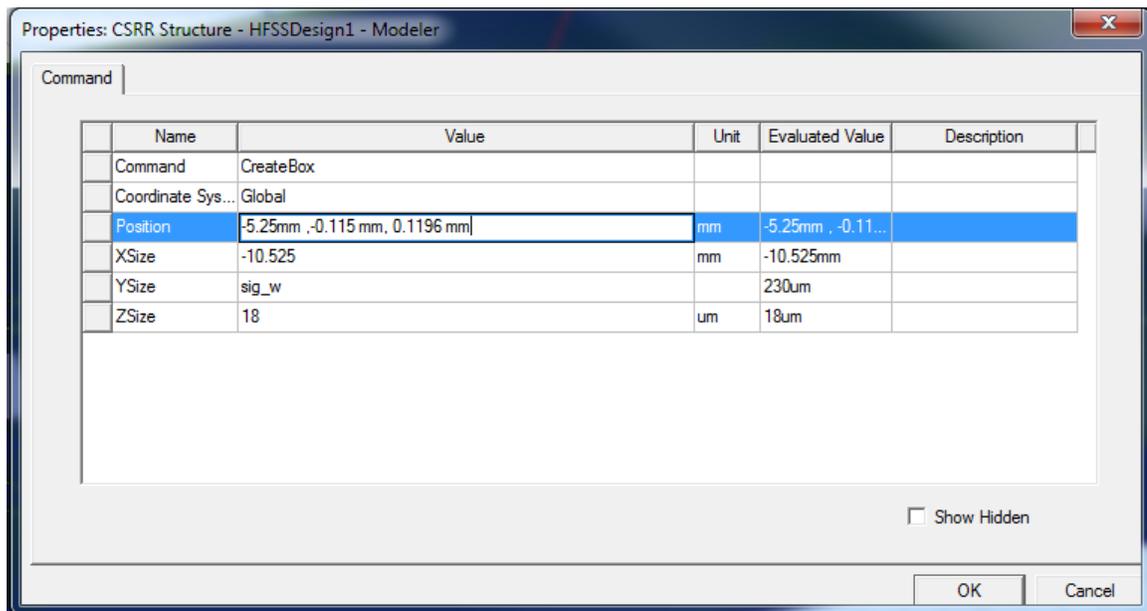
Figure 6.4. The parameter properties window used to place different HFSS constructions. It is accessed in the Project Manager window beneath the structure to be edited under "Create Box." Revisit Figure 6.3.

Simple addition and division are the most rigorous forms of arithmetic needed to actually construct a structure of stacked layers.

The CSRR etched ground plane, however, was a more cumbersome design to realize. The ground plane was just another cubic structure until Boolean operations were performed on it. Cylinders were the main tool used to "cut out" the holes that make up the CSRRs. A cylinder with a smaller radius was subtracted from a larger cylinder to form the inside ring in Figure 6.5.
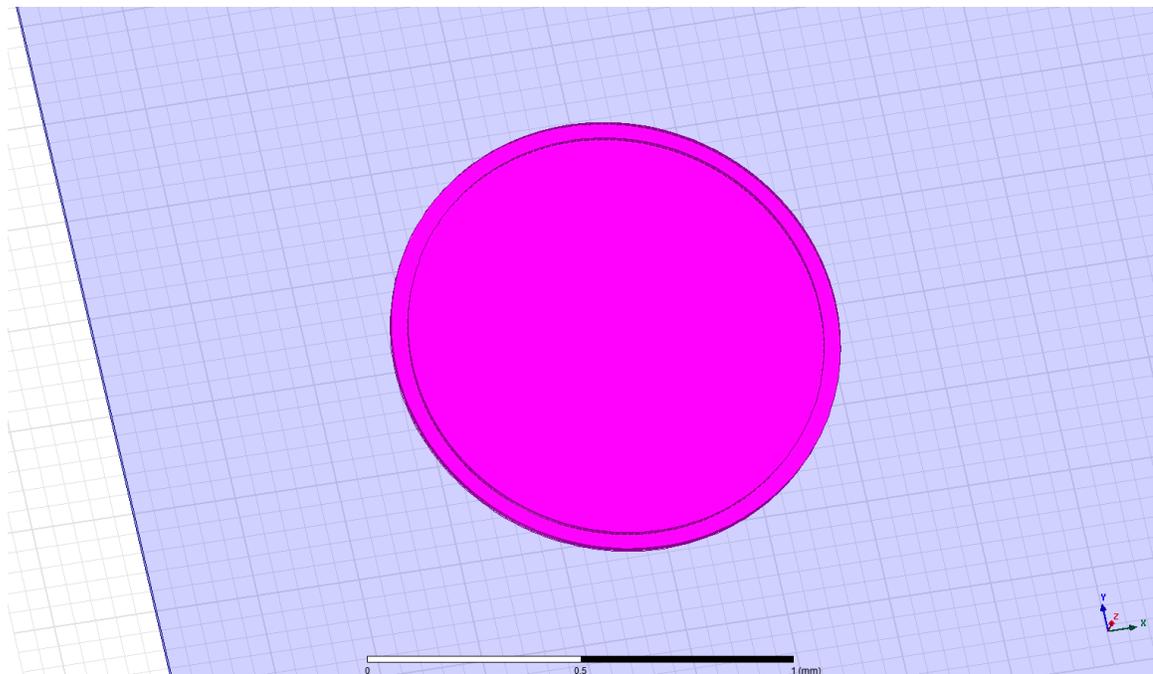
Figure 6.5a. Initial formation of the inner ring of the CSRR before subtractions were made.
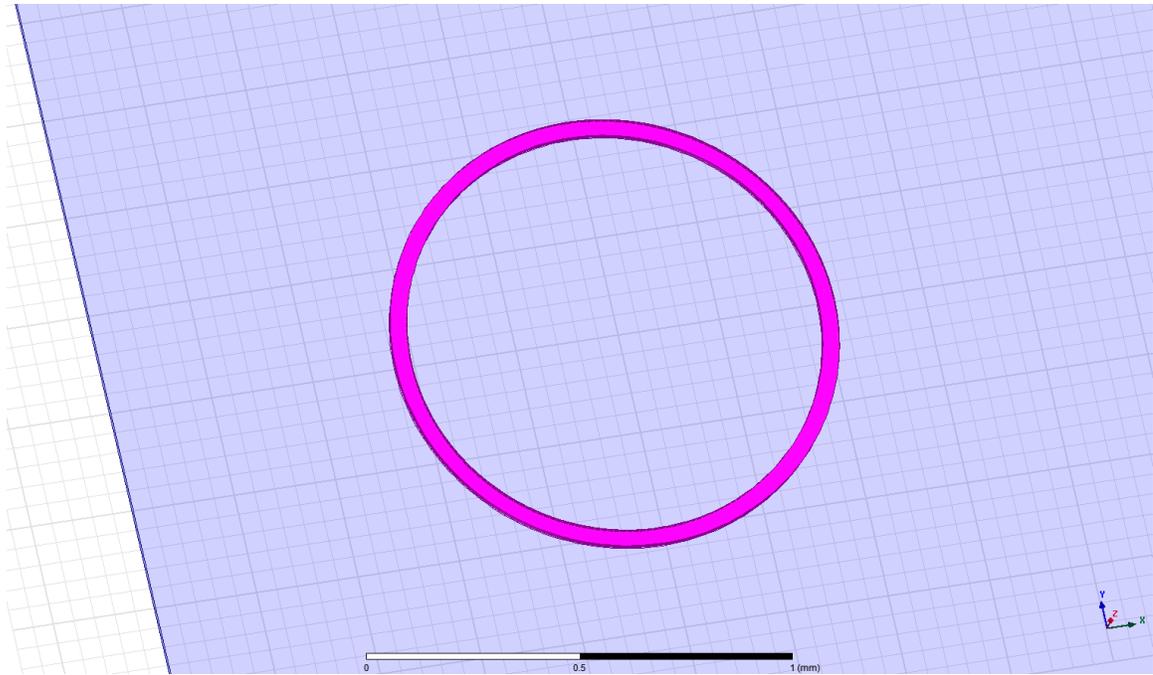
Figure 6.5b. The inner ring immediately after the subtraction of the smaller cylinder from the larger one.

Then a box was subtracted from the ring to form the gap that would serve to

induce the voltage in the ring.
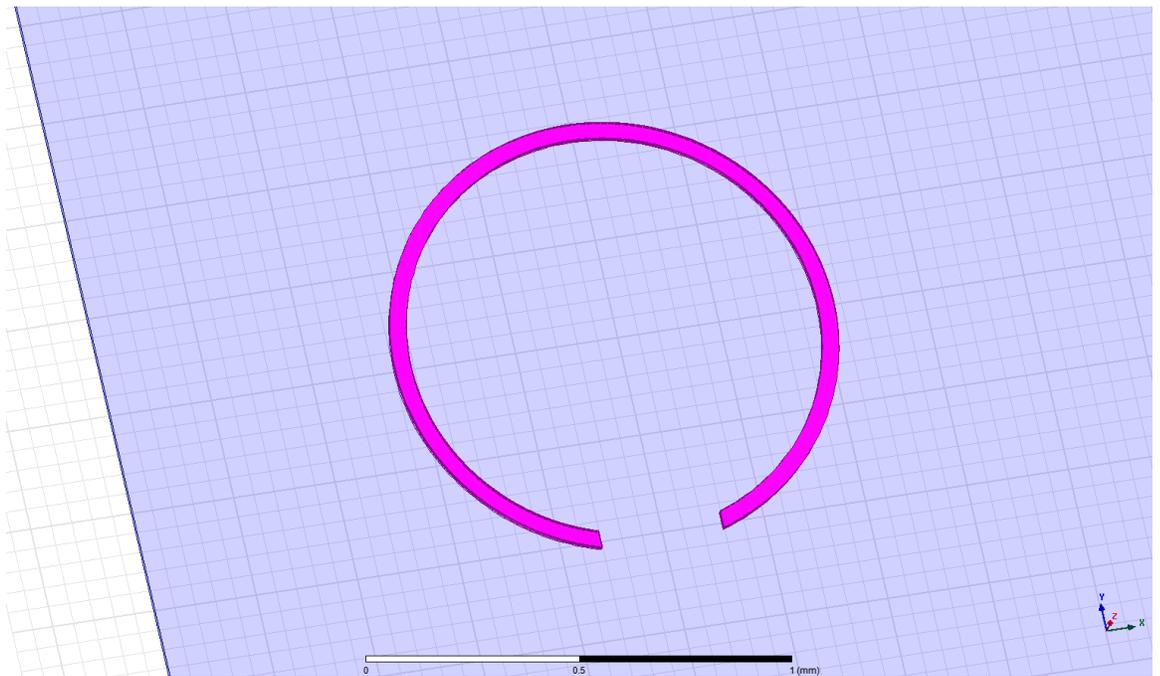
Figure 6.5c. The final inner ring configuration of the CSRR

Those subtractions produced the inner ring. The outer ring was constructed in much of

the same way. The steps are shown in Figure 6.6.
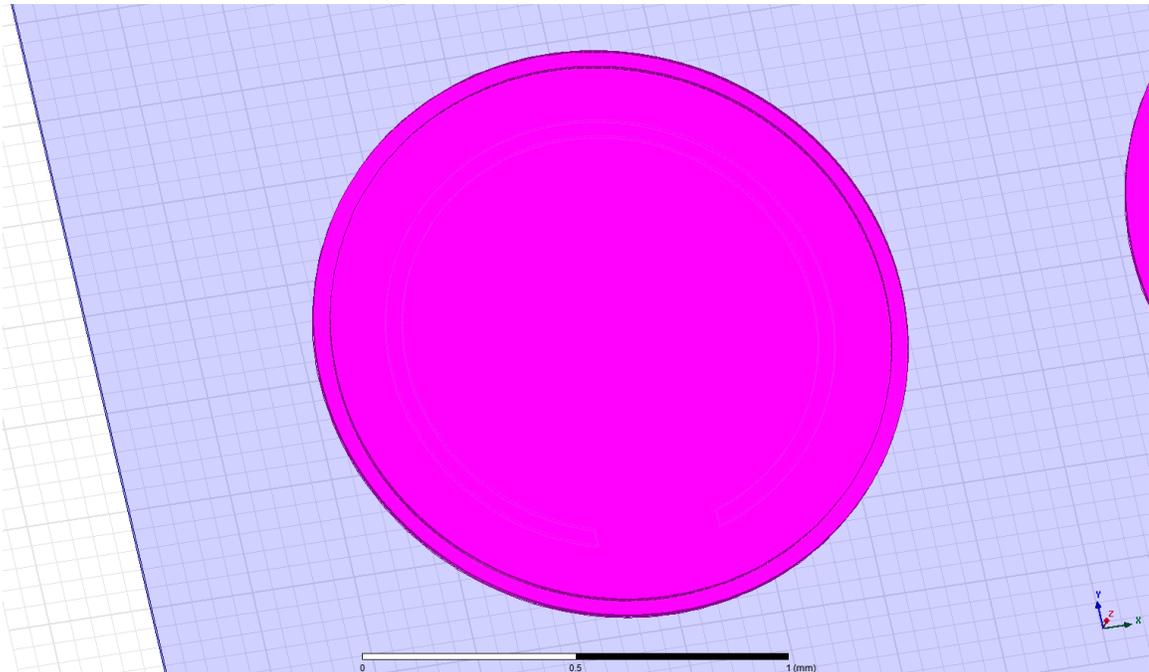
Figure 6.6a. The two cylinders used for the outer ring of the CSRR.
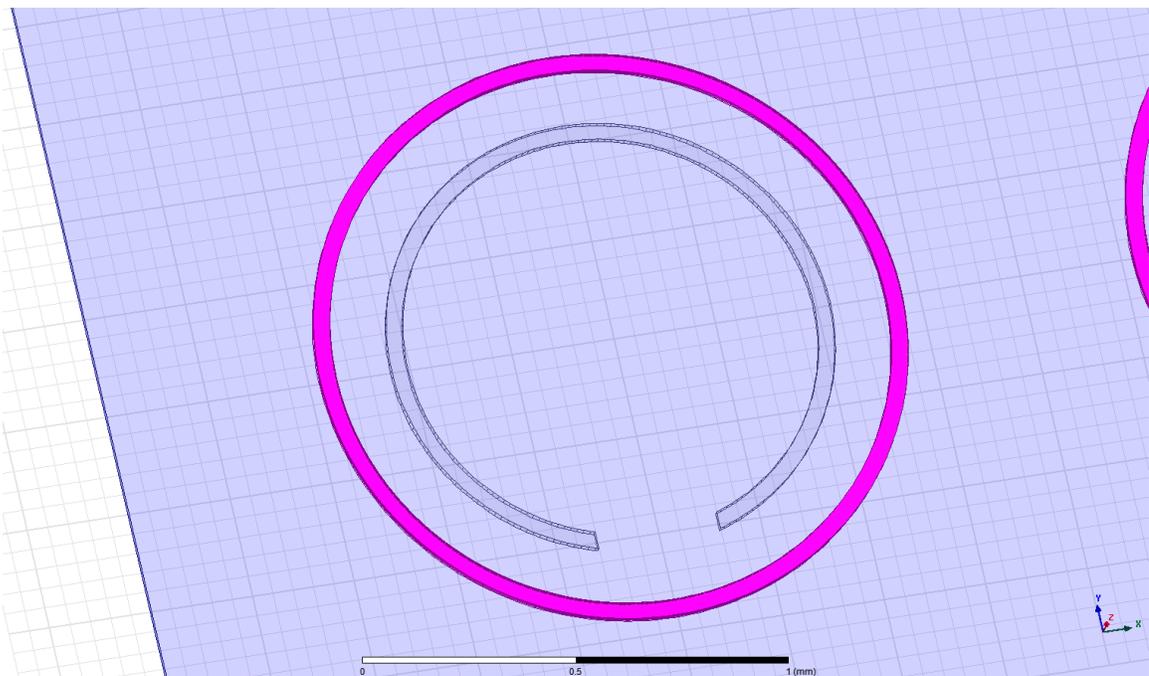
Figure 6.6b. The outer ring of the CSRR immediately after subtracting the smaller cylinder from
the larger one.
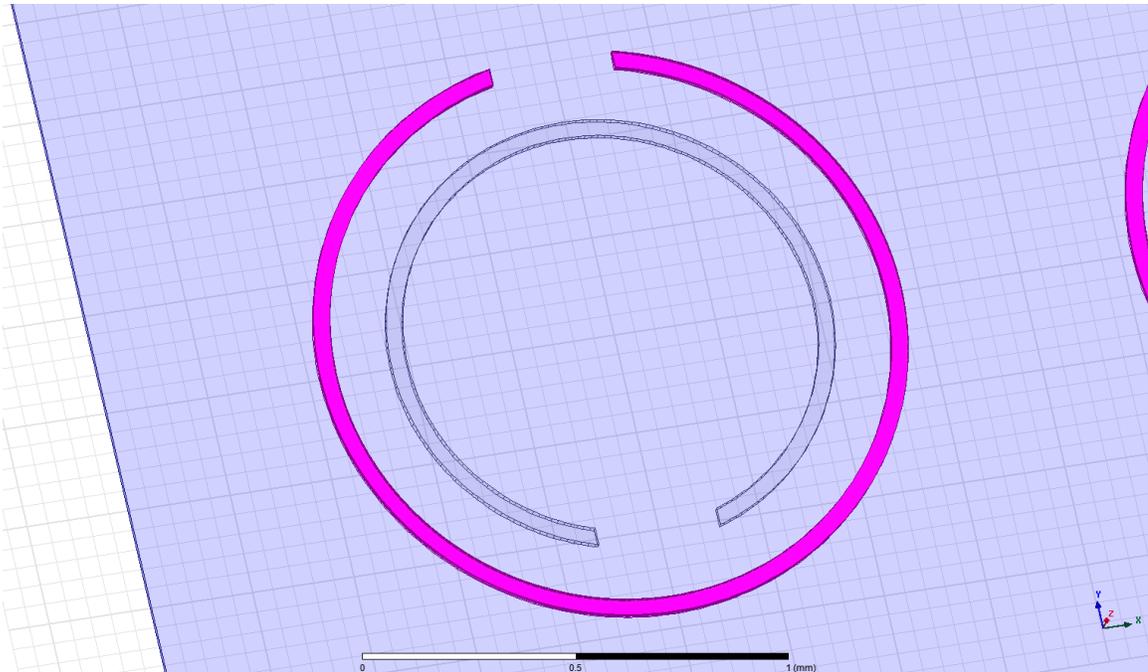
Figure 6.6c. The complete outer and inner rings of the CSRR.

Once the rings were formed, they were united into one structure and duplicated along the x-axis. The subtraction command is found by selecting the two structures, the "tool" and the "blank", and right clicking on the canvas. Then select Edit→Boolean→Subtract. A window will then appear that allows the user to specify the "tool" part and the "blank" part. The tool part can be cloned or completely absorbed into the subtraction.
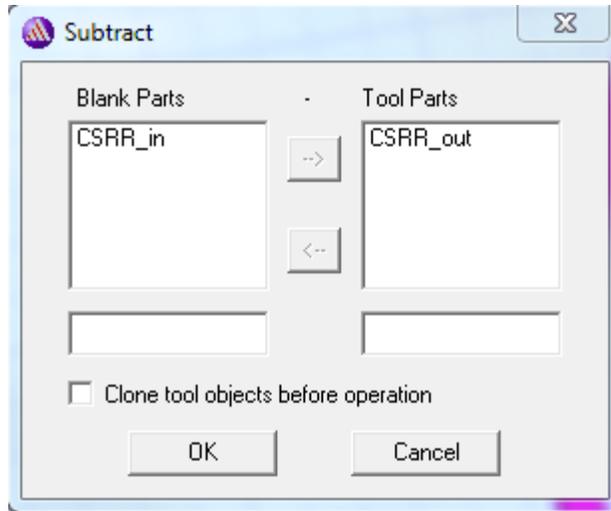
design.

The various signal layer configurations that contained capacitive gaps were

constructed in the same fashion.

Constructing a Curved Design

As stated before, the set of design parameters used for the planar designs were

also implemented in the curved designs. There is an expected margin of error in the

actual construction due to the various geometric calculations and manipulations along

with the discrepancies that were experienced in the steps between conception and

implementation in HFSS.

Taking the planar structure and simply bending it around a particular radius is not

something that can be done with a few button clicks and object selections in HFSS, it

requires the development of an entirely new structure and design. The radius needed to

form a signal length consistent with the planar case had to be calculated and then

produced using 3-D cylinders, instead of 3-D boxes. Just as they were integral to the

design of the CSRRs in the planar structures, subtractions played a significant role in the

overall design of the curved structures. Because of its complexity relative to the other two filters, the design process of the high pass filter will be explained here.

The ground plane was the first layer to be constructed in the curved design. Again, the radius of curvature of the signal layer is 3.3026 mm, which means the radius of the ground plane is 3.183 mm. Those measurements will still achieve the 119.6 μm separation between the ground plane and signal layer that is seen in the planar structure.

A cylinder with a radius of 3.183 mm and height of 4 mm was circumscribed about a cylinder with a radius of 3.165 mm. The smaller cylinder was then subtracted from the larger cylinder. This effectively gave the ground plane a thickness of 18 um. A rectangular prism with dimensions of 6.366 mm in length (along the x-axis) and 3.183 mm in height (along the y-axis) with a depth of 4 mm was used to cut the bottom half of the structure to form a semi-circular ground plane. Figure 6.8, figure 6.9, and figure 6.10 show the first three steps to creating the ground plane.
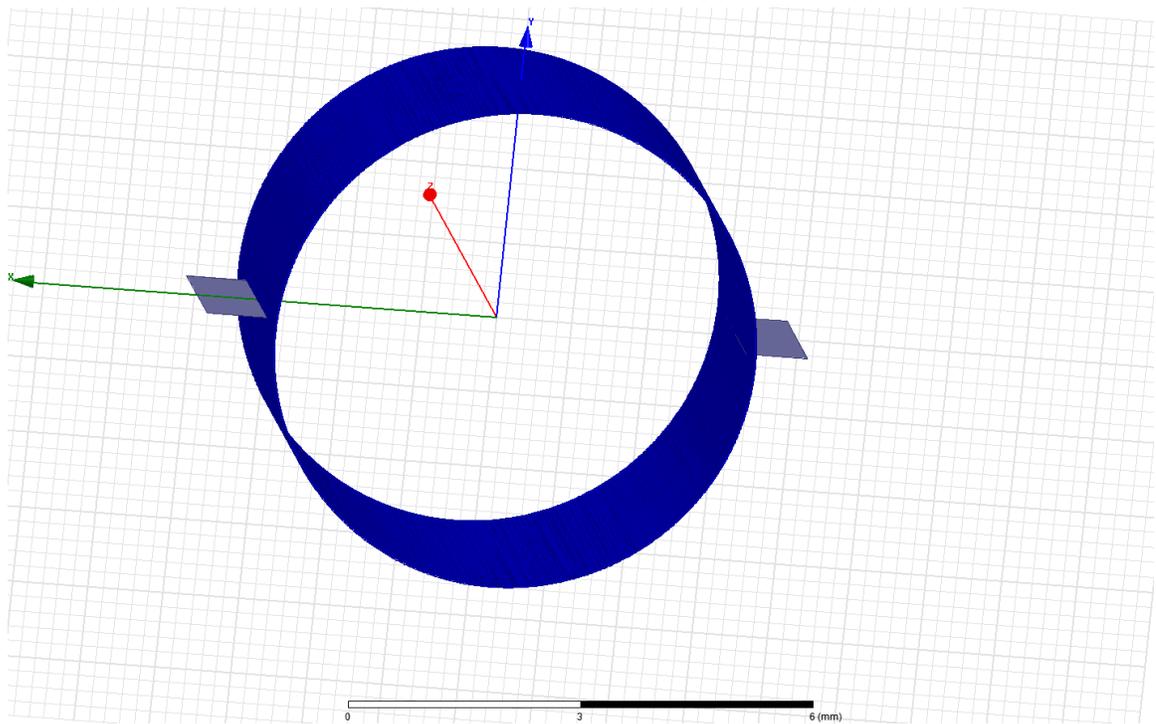
Figure 6.8. A view of the cylinder used to form the ground plane after its initial cut
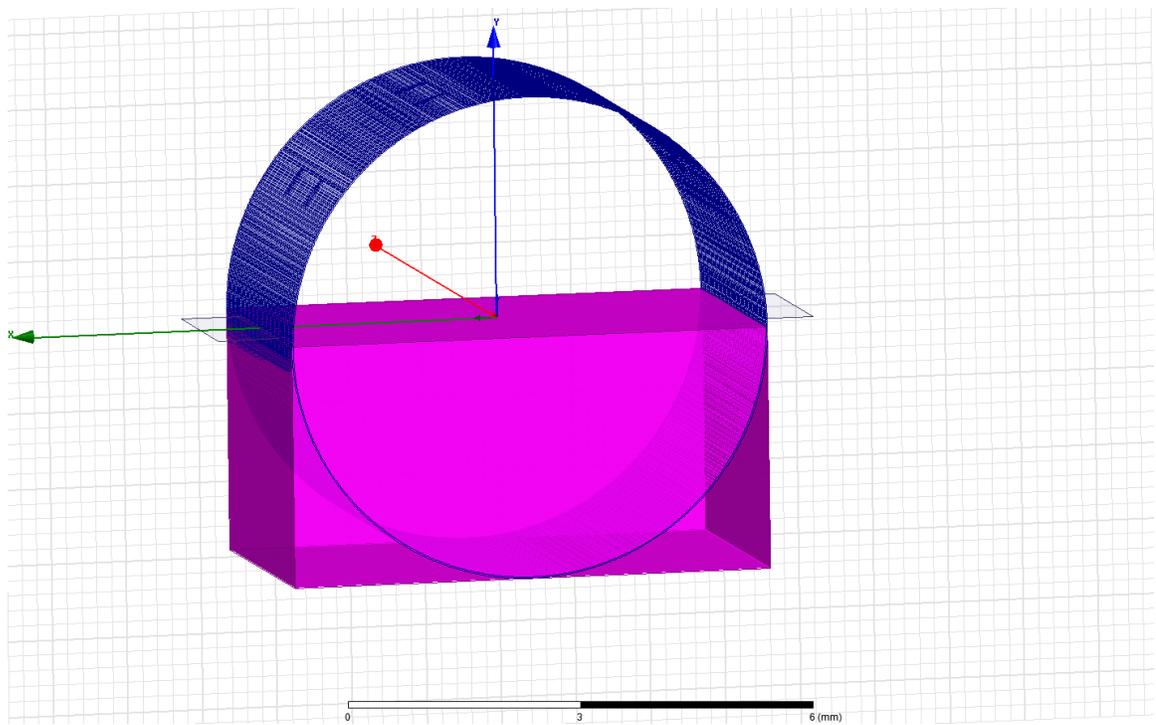
Figure 6.9. The highlighted box used to cut the cylinder in half to form the ground plane.
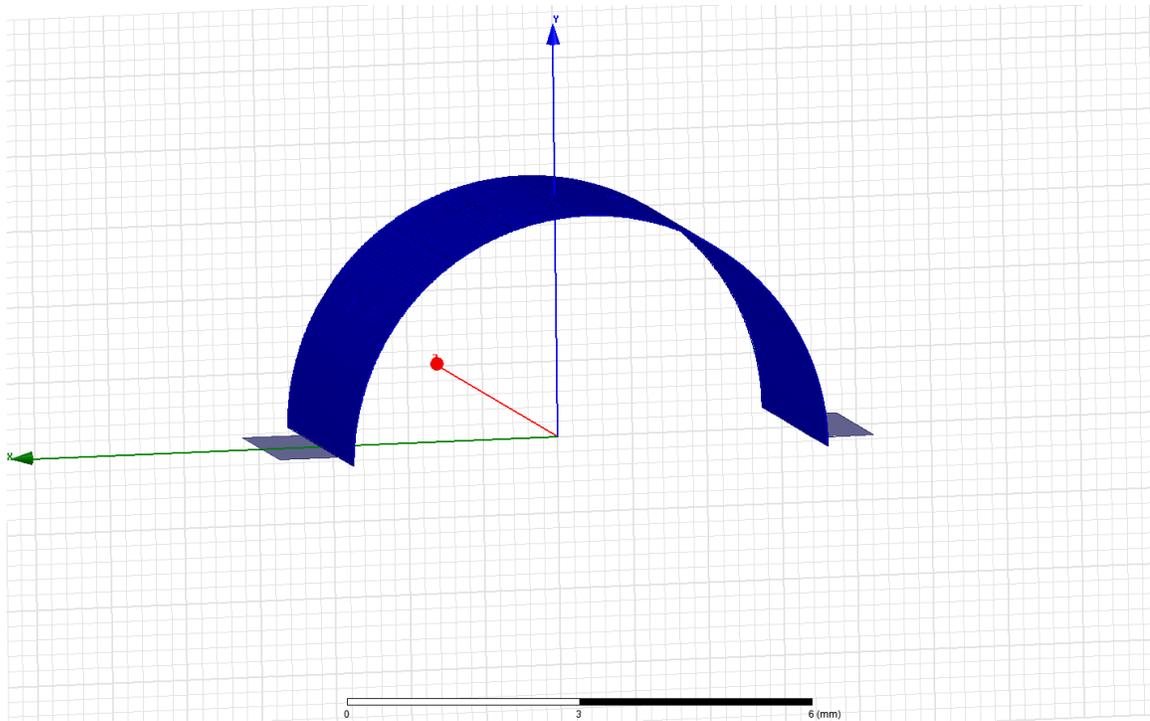
Figure 6.10. The ground plane after the box was subtracted.

Once the ground plane was formed the process of creating the CSRRs was the next step. The resonators were constructed similarly to the way they were constructed in the planar designs; they just had to be rotated at a particular angle for the curved designs. Four CSRRs are in the curved design. This was an adjustment made from the planar structure for the sake of simplicity.

Because the ground plane forms a 180 degree semicircle, the CSRRS were evenly spaced every 36 degrees. This was done by constructing one cylinder with the same dimensions as those in the planar structure, right clicking on the object, and then selecting Edit→Dupicate→Around Axis. Then four copies were made. This was done reiteratively until the inner and outer rings of the CSRR were constructed. They are shown in Figure 6.11 and Figure 6.12.

47
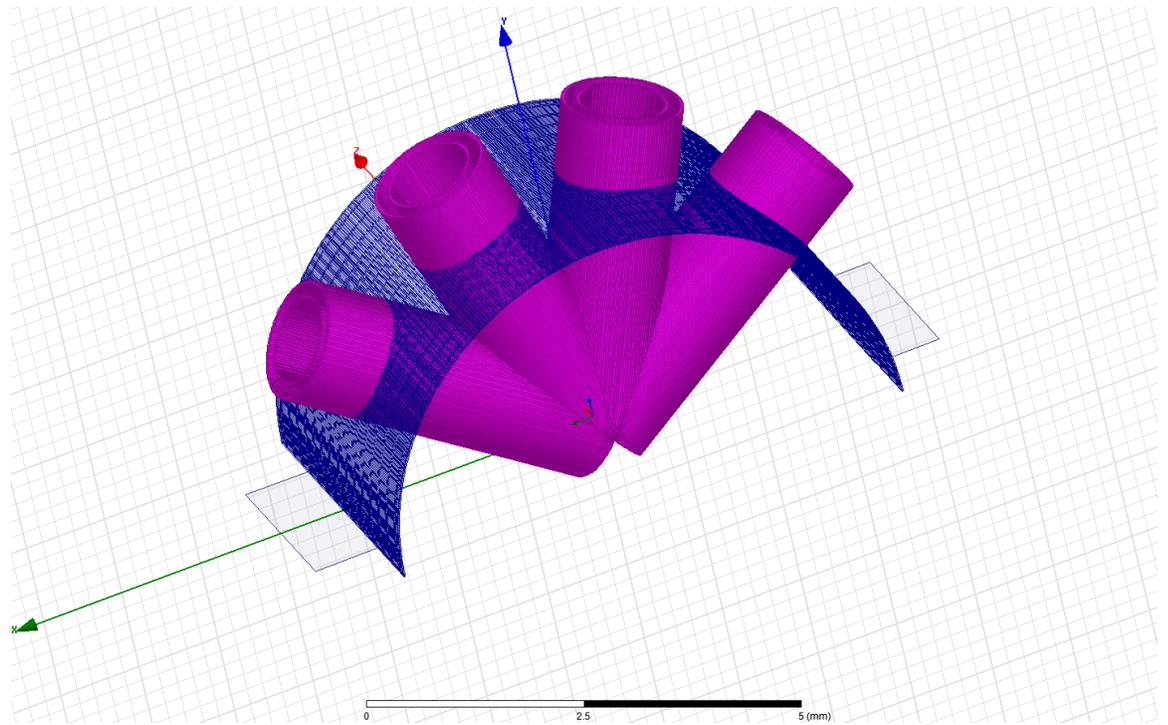
Figure 6.11. The cylinders used to form the inner and outer rings of the CSRR through the ground plane.
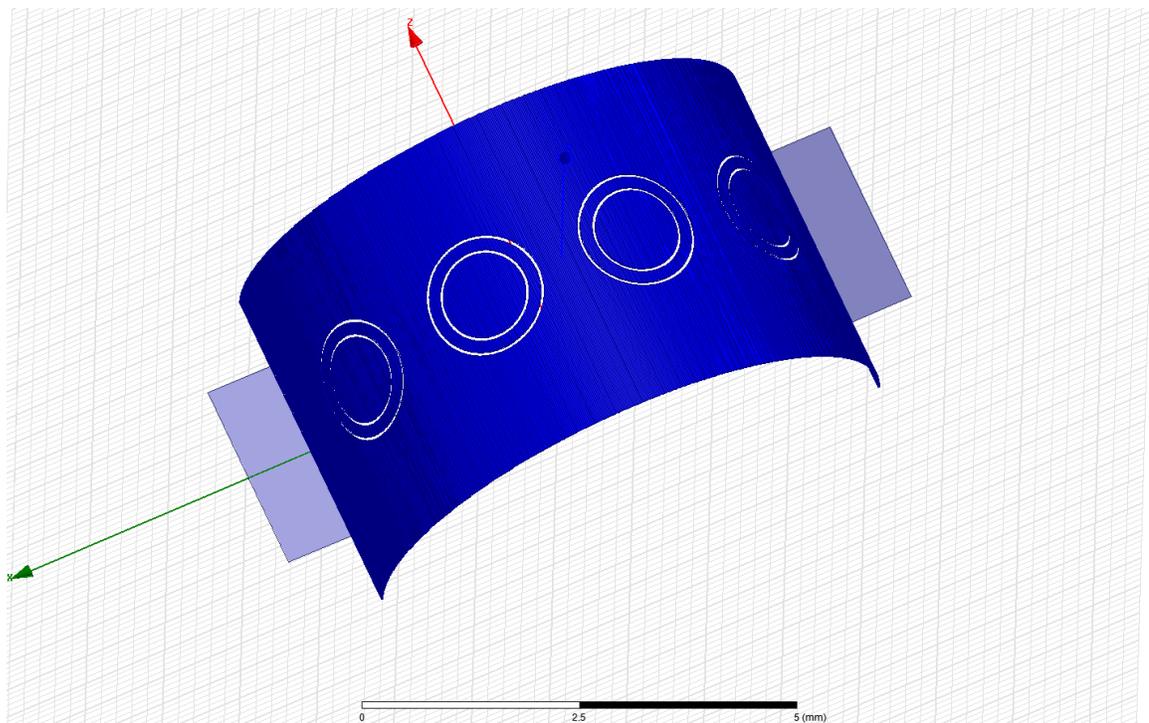
Figure 6.12. The ground plane after the CSRR cylinders were cut.

The metal gaps that were place into the CSRRS had to conform to the contours of the ground plane. So again, two cylinders were drawn with the same radius as those used to form the ground plane, but they have a height of 100 um, and the smaller one was subtracted from the larger. The bottom half of the ring was then cut followed by cutting a small section of the ring with two boxes placed on either side. This left a small segment that was later duplicated to form another segment; one for the inner ring and one for the outer ring. Both segments were then duplicated about the z-axis and rotated 36 degrees. Figure 6.13 and figure 6.14 show the segments and their placement within the CSRRs.
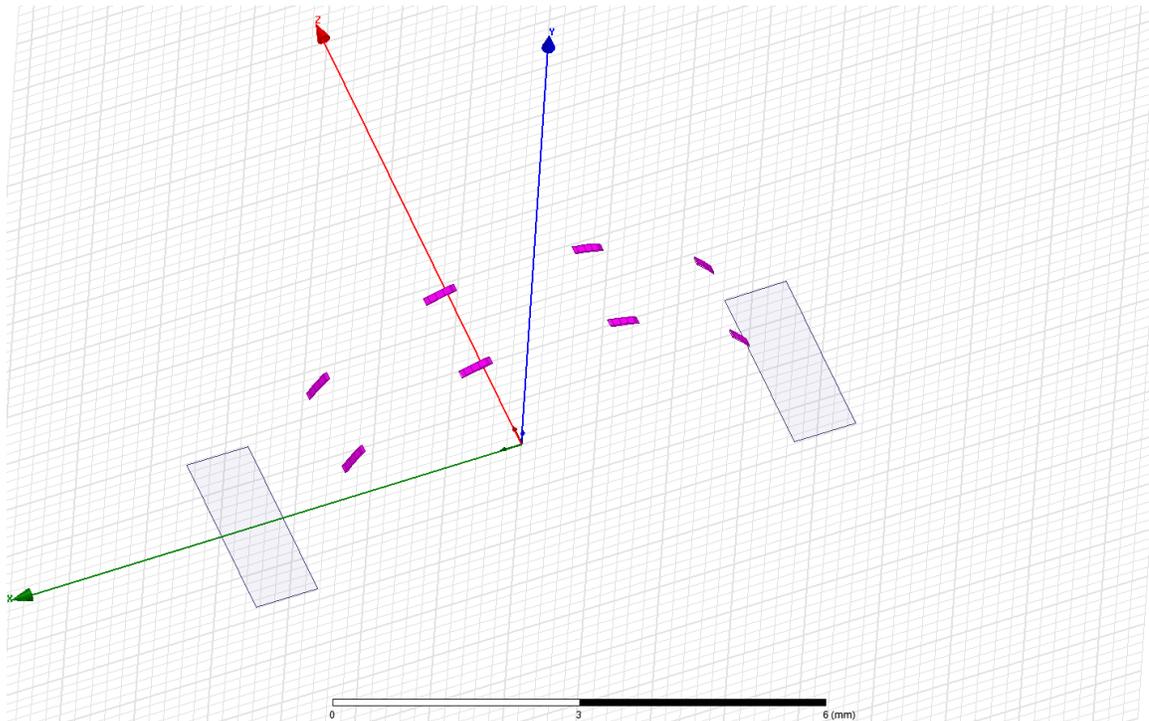
Figure 6.13. The small segments used to form the metal ground layer gaps in the CSRRs.
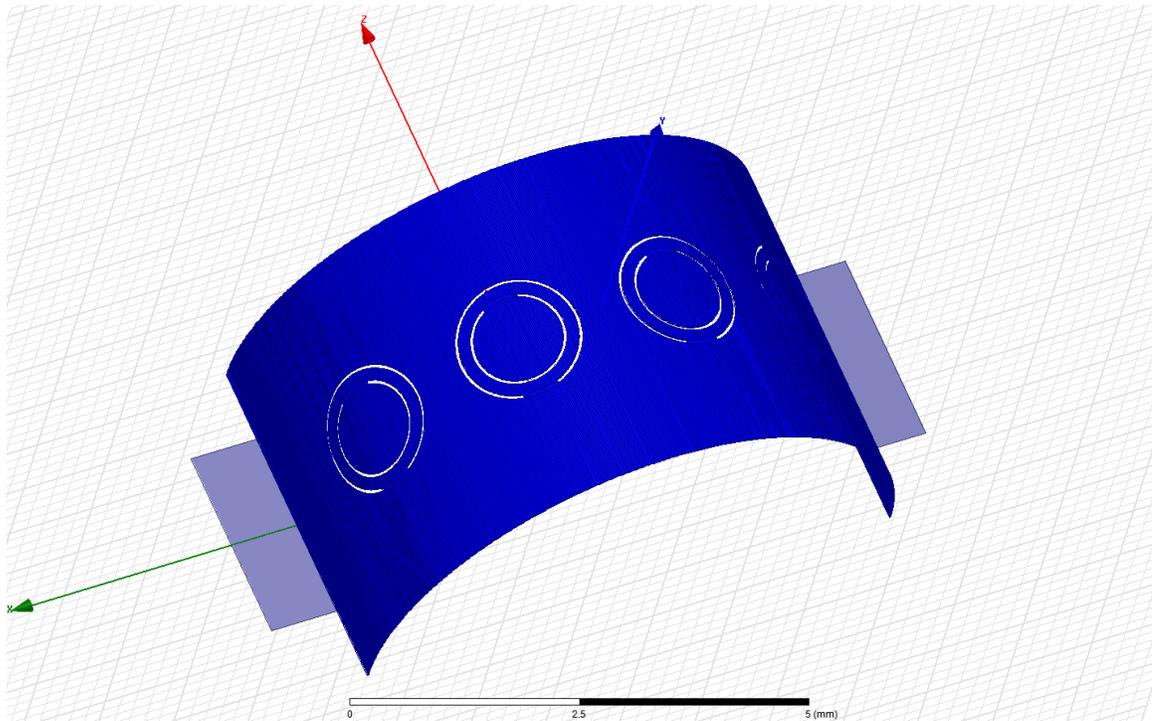
Figure 6.14. The complete ground plane with CSRRs.

The substrate layer was then drawn on top of the ground plane. A procedure similar to

forming the ground plane before the CSRRs were placed was used for the substrate layer.

Two cylinders were drawn and the smaller one was subtracted, which formed a ring that

was later cut in half by a box. In this case, the larger and smaller cylinders had radii of

3.2846 mm and 3.183 mm, respectively, in order to form a substrate with a thickness of

101.6 um, just like the planar structure. Figure 6.15 shows the substrate and ground
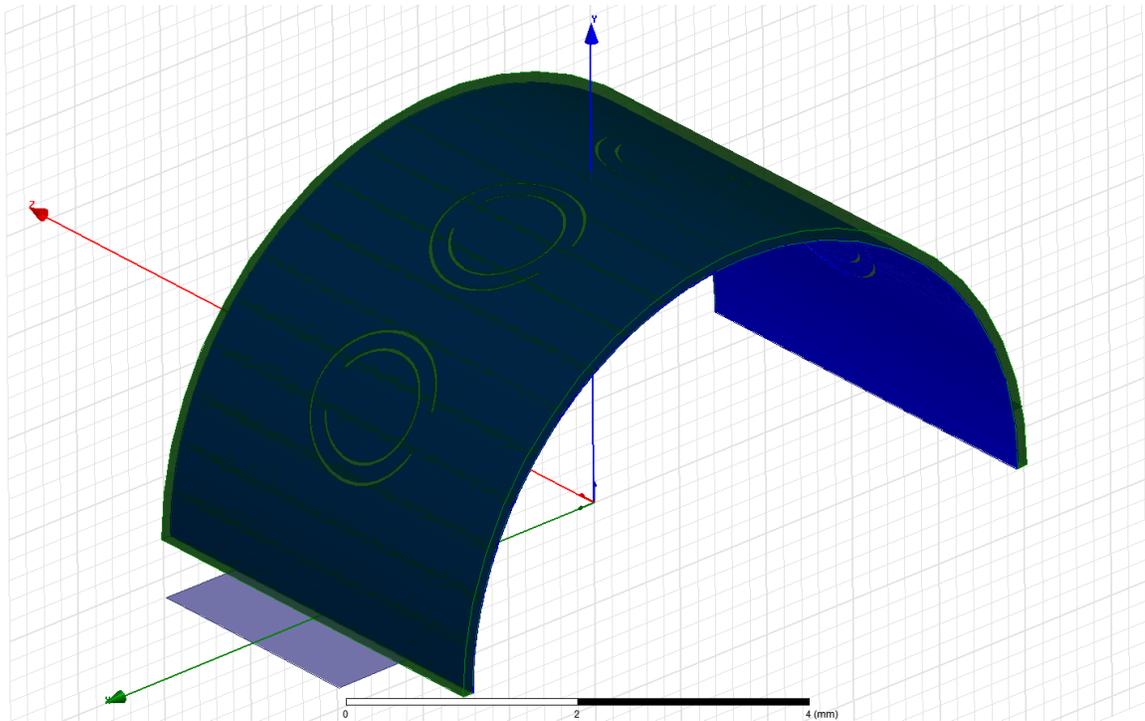
plane.

Figure 6.15. A view of the substrate layer overlapping the ground plane.

The most difficult part of this construction was the signal layer. The signal layer was drawn with two cylinders and a box, just like the substrate and ground. The cylinders had a radius of 3.3026 mm and 3.2846 mm. The signal has a thickness of 18 µm after the smaller cylinder was subtracted from the larger. To maintain the signal width, the height of the cylinders is 230 µm. Their centers were placed at -115 µm on the z-axis to ensure the signal would lie in the center of the structure.
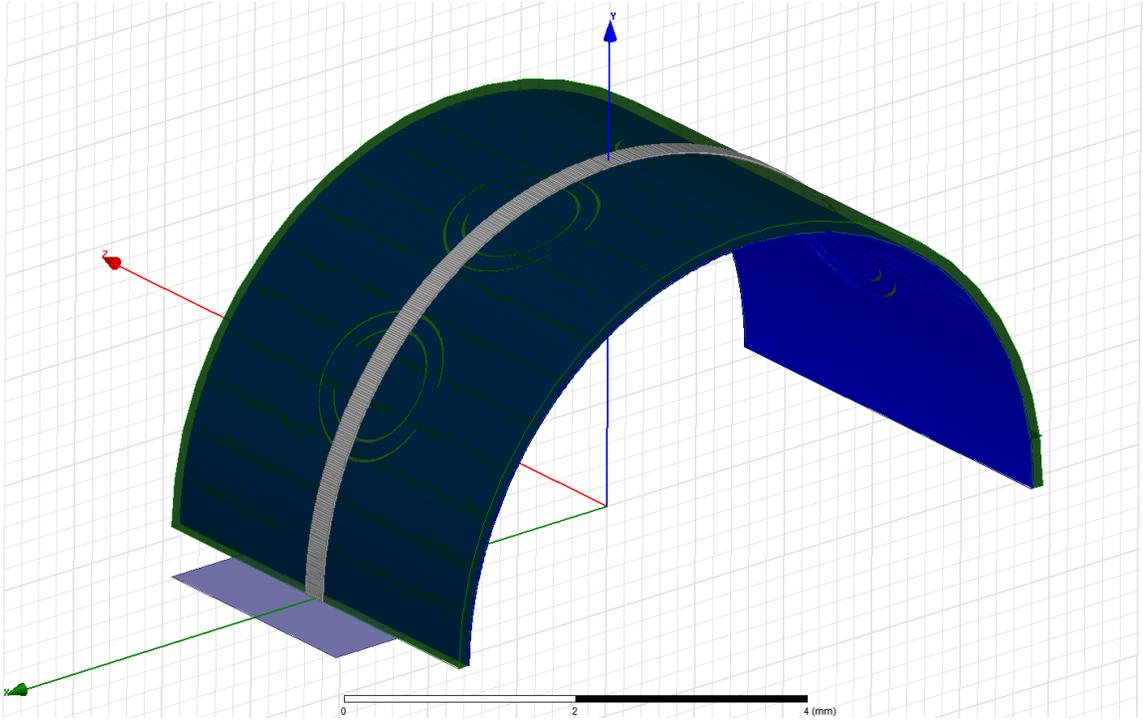
Figure 6.16. The signal trace placed on top of the ground and substrate layers.

After the signal was formed, the high pass components were drawn. Recall the signal

trace of the planar structure has gaps with elongated pieces of metal on either side. These

gaps and pieces of metal follow the contours of the signal layer's arc. To create the gaps,

a box with the dimensions of the gaps in the planar structure was drawn on the x-axis. It

was then duplicated around the z-axis and placed every 36 degrees.
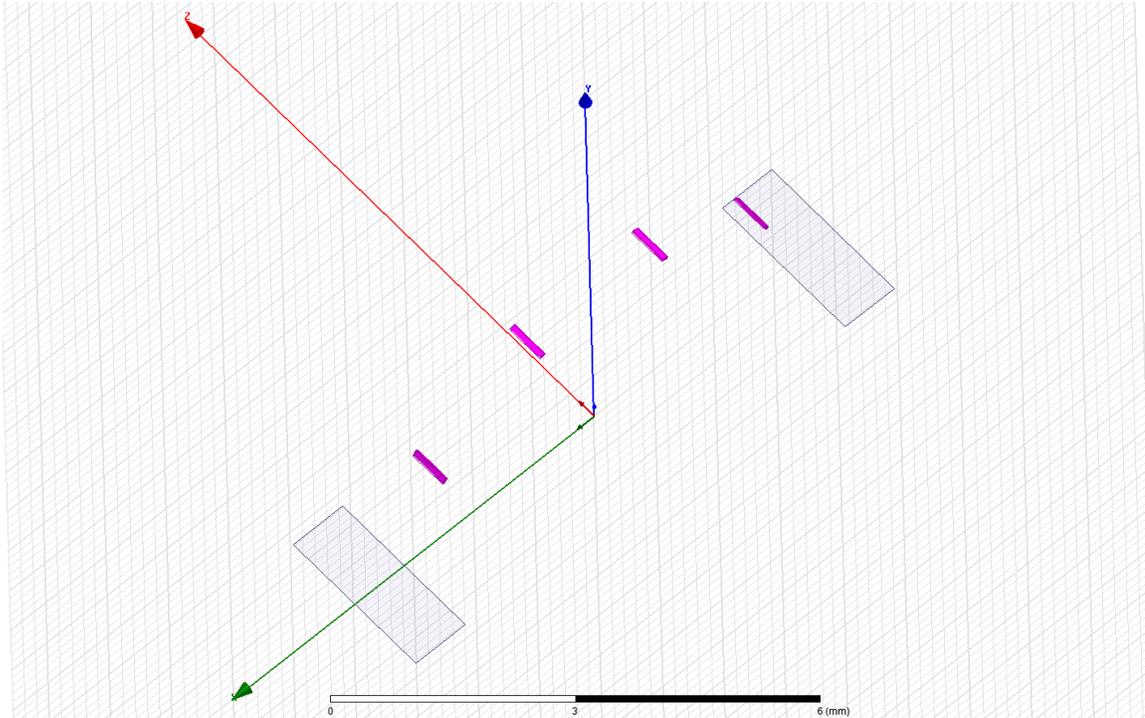
Figure 6.17. The boxes used to form the gaps in the signal layer.

The pieces of elongated metal were made by using a similar procedure of cylinders and boxes. The cylinders have the same radii as the two cylinders used to design the signal layer, but they have a height that is 550 um in order to be consistent with the lengths of the metal pieces in the planar structure. After the initial subtractions, the simplest way to actually form the metal pieces was to make several cuts with several boxes. Figure 6.18 and figure 6.19 give an idea of how they were formed.
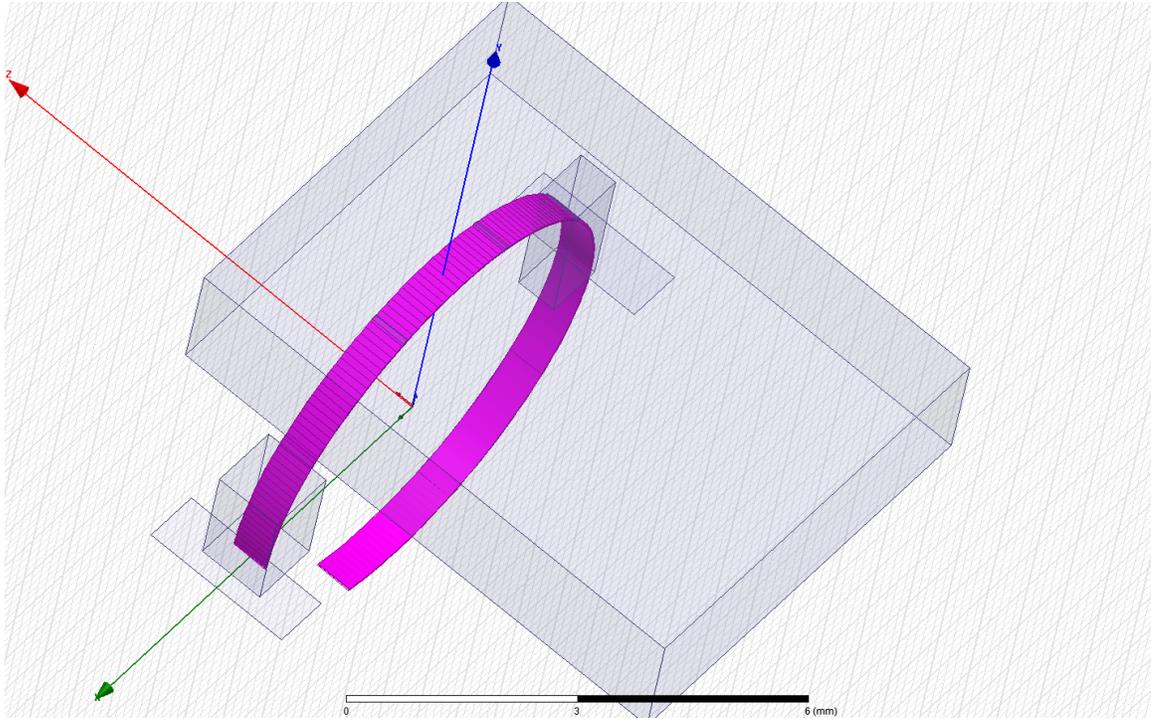
Figure 6.18. The ring and boxes used to form the elongated metal pieces before subtractions were made.
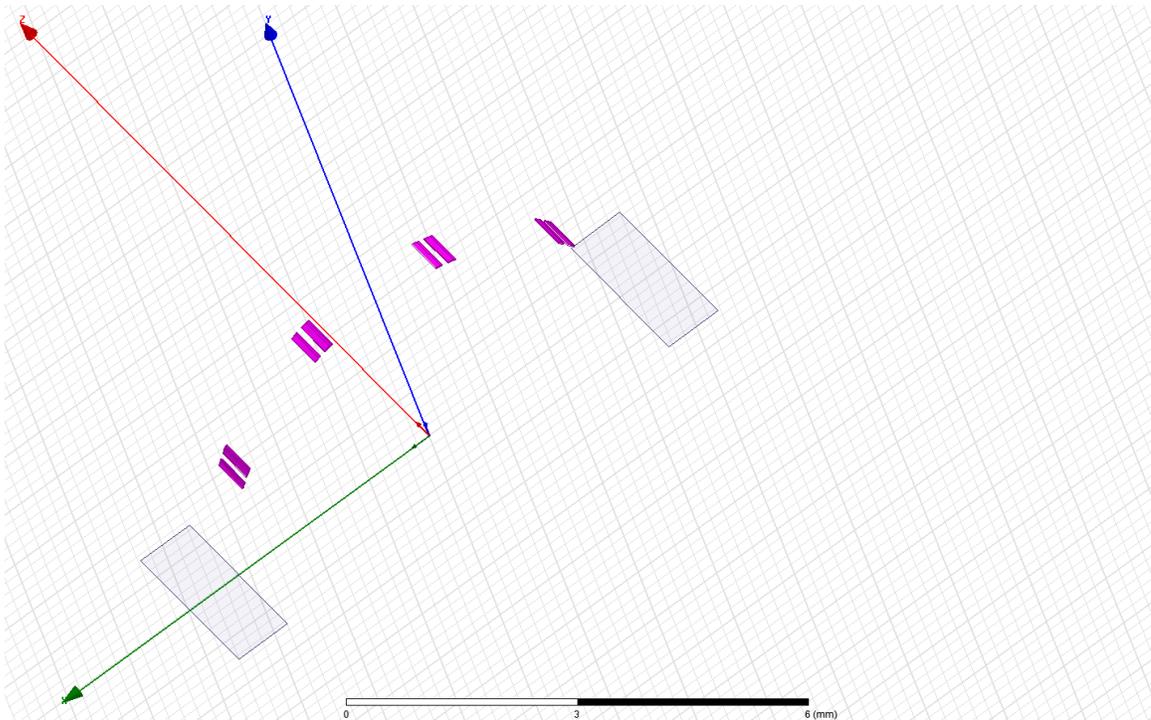
Figure 6.19. The elongated metal pieces that lie on the signal line.

54
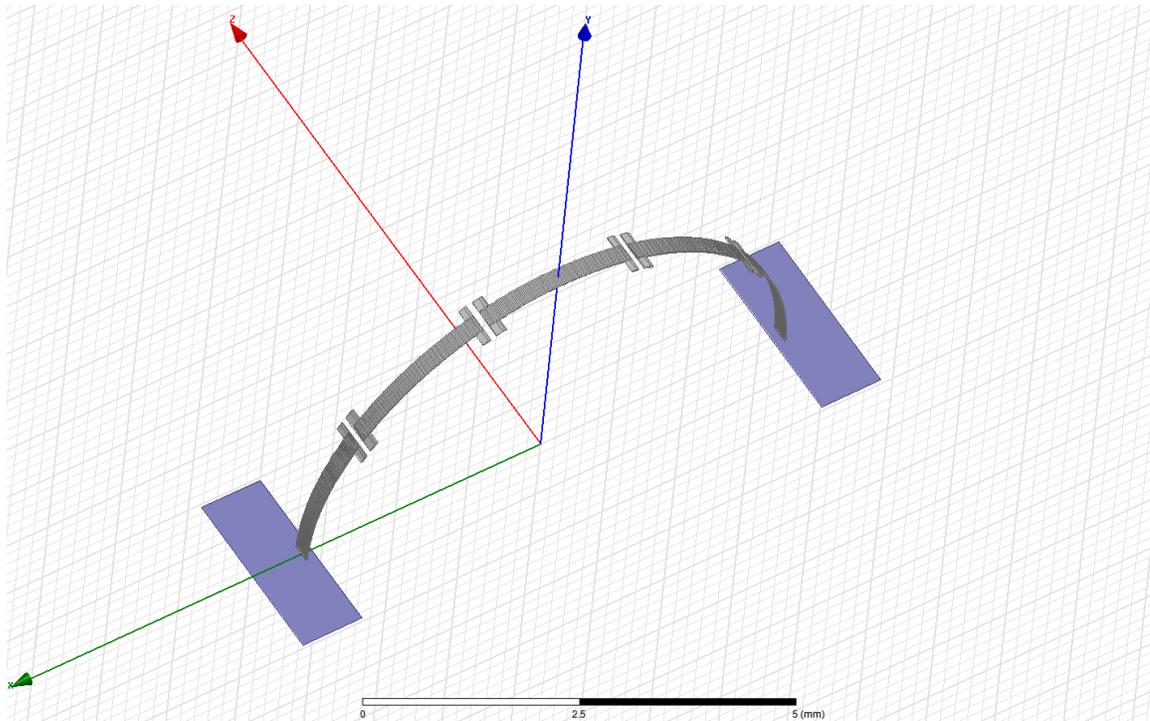
Figure 6.20. The complete high pass signal layer.

The signal lines needed for the band stop and band pass filters are intrinsic to the design of the high pass filter. Minor subtractions and non-model object selections will produce either signal trace.

Simulating a CSRR loaded transmission line structure such as these, whether curved or planar, in HFSS is markedly different from simulating a simple microstrip transmission line. The following chapter will address how to simulate a CSRR loaded transmission line.

55

Chapter 7
HFSS Simulation

    HFSS requires its users to be aware of several things when attempting a simulation. Errors can range from intersecting/overlapping structural layers to improper boundary configurations. Simulating a CSRR loaded transmission line even requires the user to consider meshing techniques, but the most important simulation features are boundary condition, frequency analysis settings, structure material definitions, and excitation ports.

    The first step to simulating the structures was to define the simulation region. A region box was drawn around the structure which then had a radiation boundary applied to it. The box's size was determined by measuring $\lambda/4$ mm away from the transmission line's upper and lower surfaces. The radiation boundary is applied by selecting the box that surrounds the structure and right clicking. Then select Assign Boundary→ Radiation→ OK.
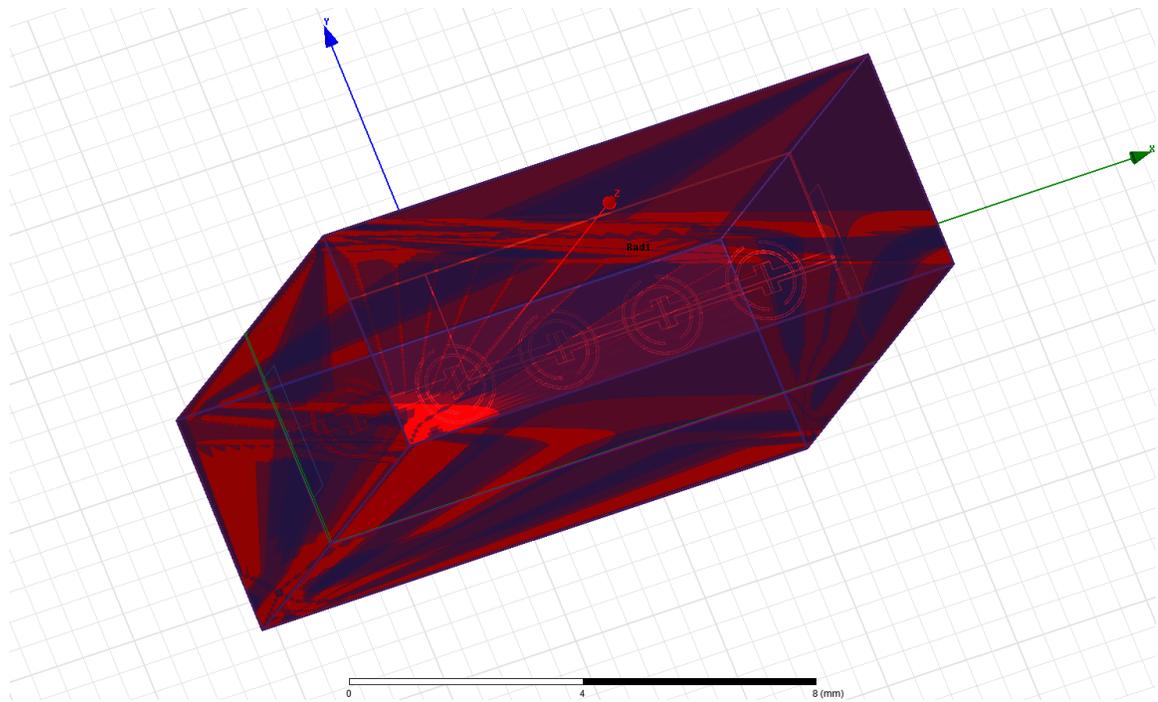
Figure 7.1. The radiation boundary that surrounds the CSRR loaded transmission line

After the radiation boundary is in place, the next step is to define the excitation

ports. The first step to doing this is to draw 2-D rectangles that are 10 times the signal

width and 8 times the substrate height. The bottom of the rectangle should touch the

bottom of the ground layer and should extend past the signal layer. The box should be

coplanar to the terminated edge of the signal. Rectangles such as the one described

should be drawn on either end of the transmission line. When the positions of the

rectangles are set, an excitation is assigned to each one independently of the other.

Simply select the rectangle, right click, and select Assign Excitation → Wave Port (in this

case). Because this particular simulation is driven modal, the most important component

to assigning excitations is to define the integration line. The line determines the largest

voltage difference in the simulated structure, which is typically between the ground plane

and the signal layer. The line should be drawn from the top center of the signal line

(denoted with a green triangle) to the bottom center of the ground plane. The next step in

the excitation assignment window is to select "Renormalize Ports". Figure 7.2 shows the

excitation ports and integration line assignment window.
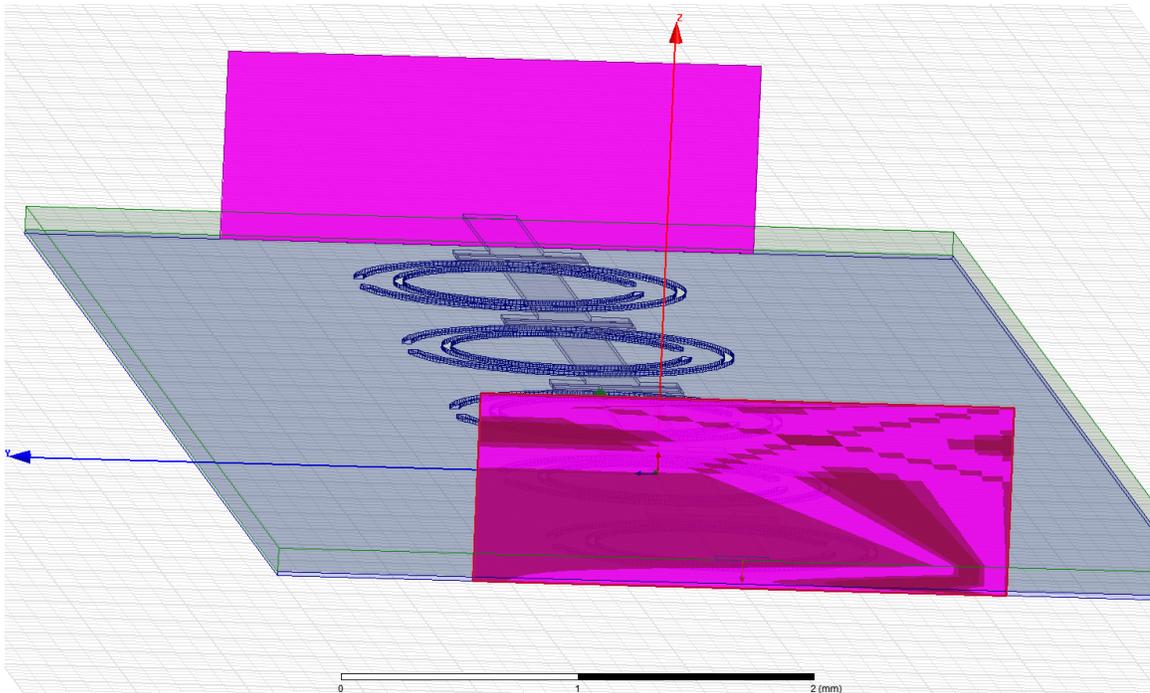
Figure 7.2a. The rectangles used to designate the structure's excitation ports.
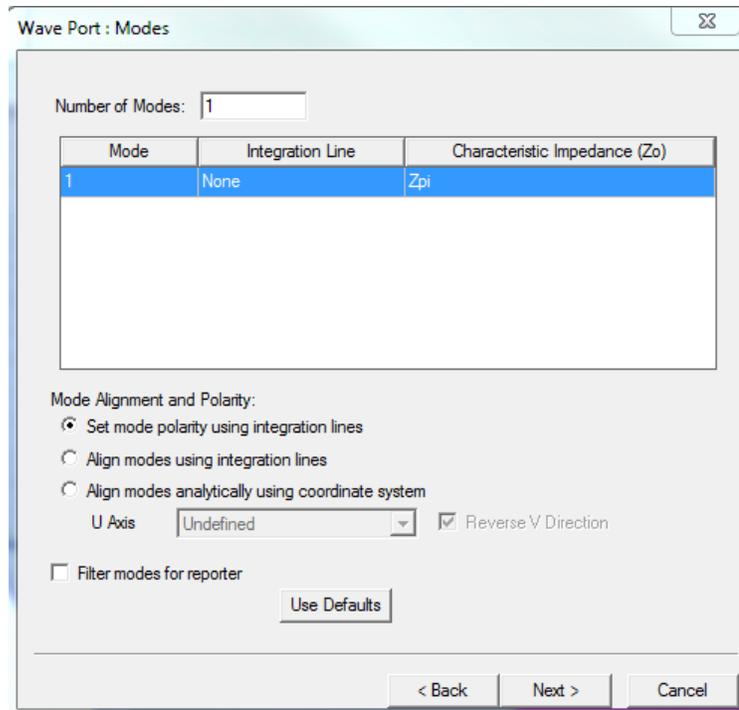
Figure 7.2b. Integration line definition. Click the drop down menu under integration line, select new, and draw the line on the structure.
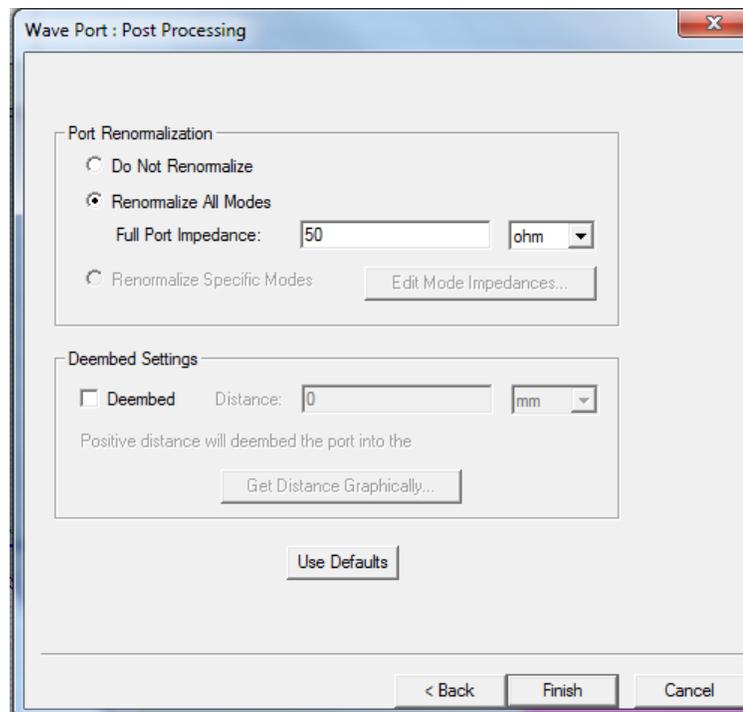

Figure 7.2c. Port modes. Select renormalize all modes and set it to 50 ohms.

After the excitations have been set, the next step is to configure the frequency analysis. In the Project Manager window on the left side of the screen, "Analysis" is right-clicked and Add Solution Step is selected. A solution step window will then appear.
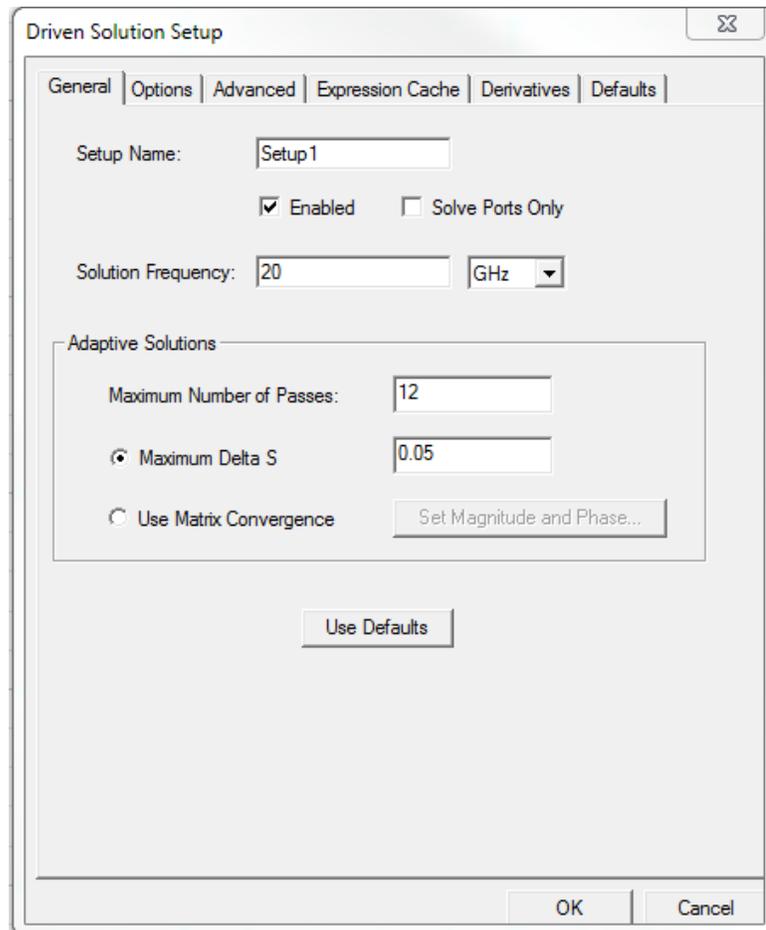

Figure 7.3. The solution step window used to regulate the simulator's operating regime.

The solution frequency is chosen to be near the structure's resonance. The maximum number of passes under Adaptive Solutions controls how many times the simulator will attempt to force the calculations to converge. Maximum Delta S determines how much error is allowed in the simulation.

After the solution setup is finished, a frequency sweep is added by clicking on the red line graph in the toolbar. For this simulation, the sweep type is interpolating and the frequency step is a linear count of 201 points between 10 GHz and 30 GHz.
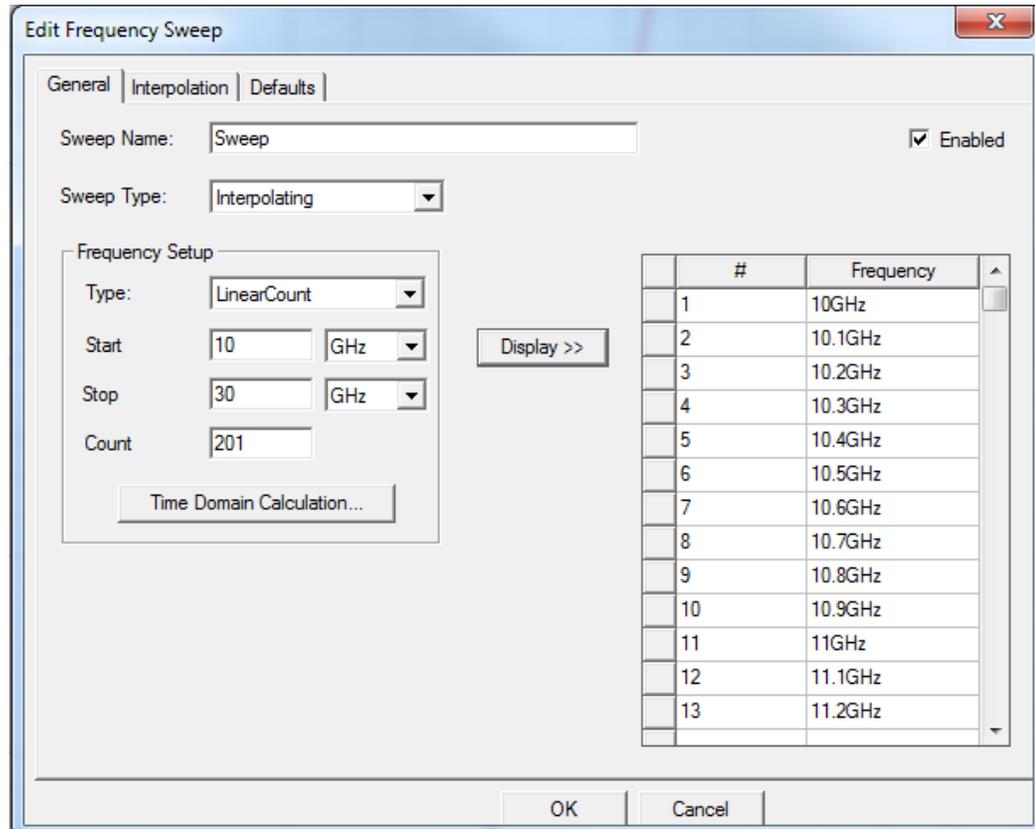

Figure 7.4. The frequency sweep window where the user applies the evaluated frequency range.

The final step in setting up the simulation is configuring the results page. The Results menu is found in the Project Manager. After right-clicking on Results, Create Modal Solution Data Report → Rectangular Plot is selected. The Report window is then generated, which is where the user can choose which set of parameters are to be analyzed. The S Parameters S_{11} and S_{21} were chosen for this simulation. A tab is generated under Results in the Project Manager window after "New Report" is clicked on the Report window.
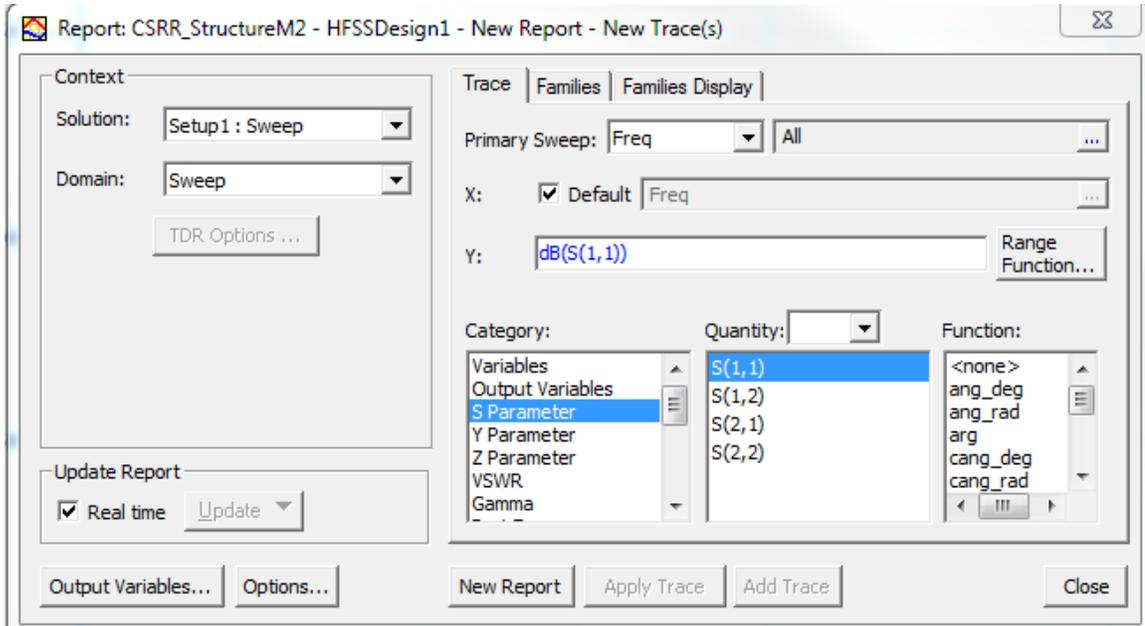
Figure 7.5. The Solutions Report window where S Parameters are selected for evaluation.

These simulation steps were performed repeatedly to evaluate the three filter designs that will be discussed in the following chapter. Not only were these steps completed for planar structures, but also for those that were curved. Assigning excitation ports and simulating the curved structures are done exactly as they are done for the planar structures. The ports will just lie along the x-axis and z-axis.

Chapter 8
Filter Simulation Results

As stated before, three types of CSRR loaded transmission line filters were designed and simulated in HFSS: high pass, band stop, and band pass. Each filter was simulated twice; once as a planar structure and again in a curved form. The liquid crystal polymer substrate intrinsic to the filters' designs is a flexible dielectric that will allow the filters to be bent various radii. The objective of the simulations is to compare the frequency response of the planar structures to the curved structures in hopes that their scattering parameters would be similar. The filters, both planar and curved, their return loss, and their insertion loss are displayed and their results described below.

Figure 8.1 is another depiction of the planar high pass filter along with its insertion loss and return loss. The transmission line begins to discern high frequencies at approximately 17.5 GHz. The filter's insertion loss at its high pass region is approximately -3 dB.
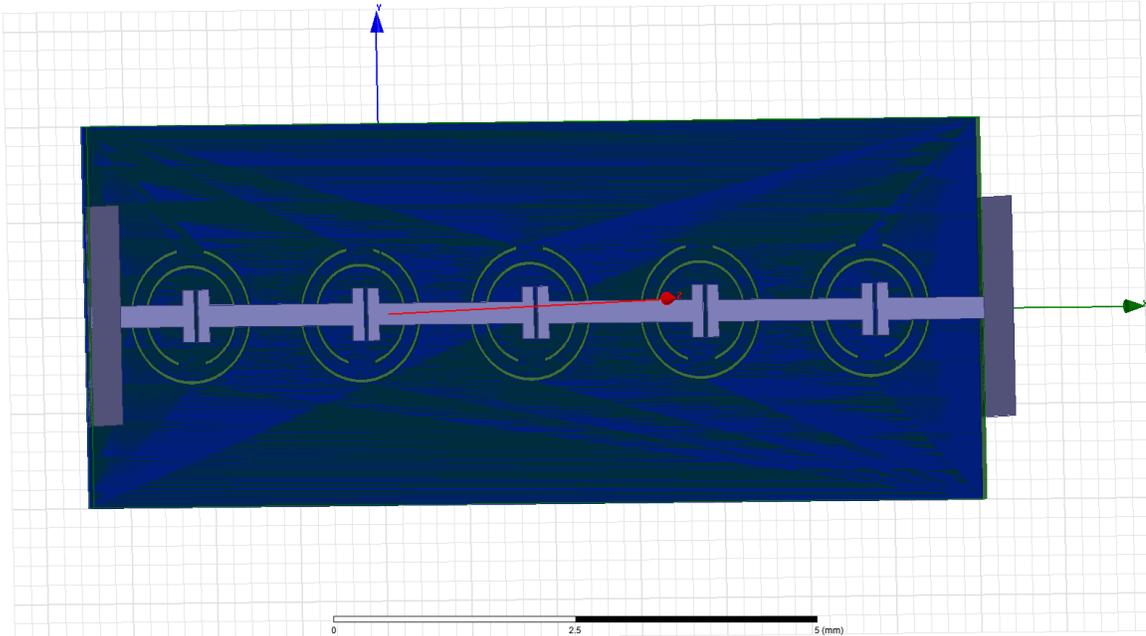
Figure 8.1a. Planar high pass filter design
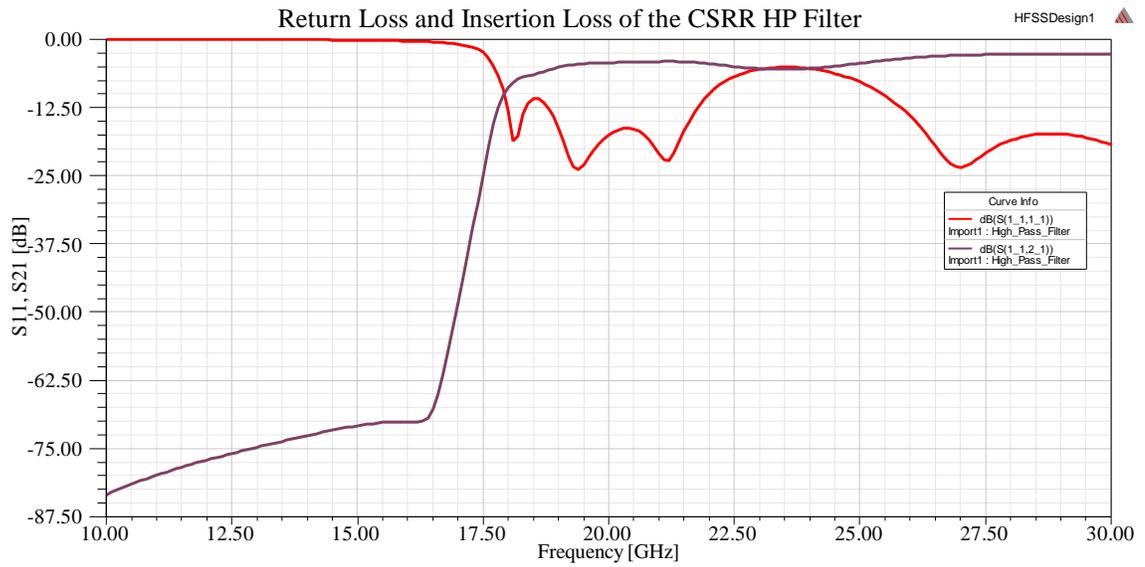
Figure 8.1b. Return loss (red) and insertion loss (purple) results of the planar high pass filter

Figure 8.2 is a depiction of the planar stop band filter along with its insertion loss

and return loss. The stop band of frequencies is between 18 GHz and 22 GHz. The

insertion loss is a lot more robust at the lower frequencies than at the higher ones.
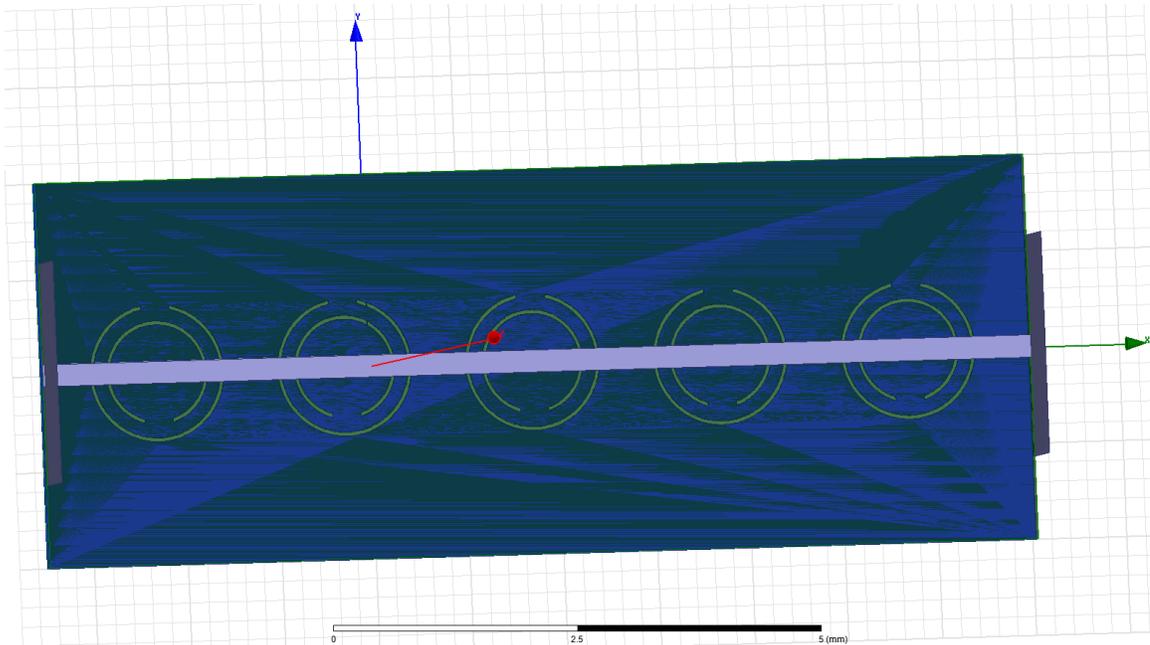
Figure 8.2a. Planar band stop filter design
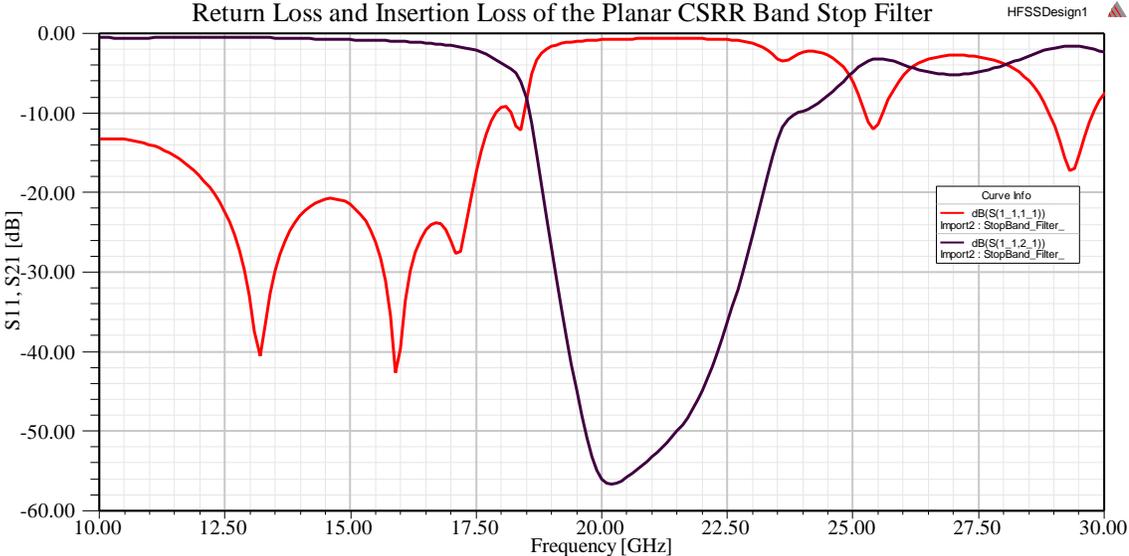
Figure 8.2b. Return loss (red) and insertion loss (purple) results of the planar stop band filter

Figure 8.3 is a depiction of the planar pass band filter along with its insertion loss

and return loss. The pass band of frequencies is between 18 GHz and 22 GHz. The

insertion loss does not decrease as strongly in the higher frequency range, but the filter

will suffice as a band pass. The insertion loss does fall below -20 dB.
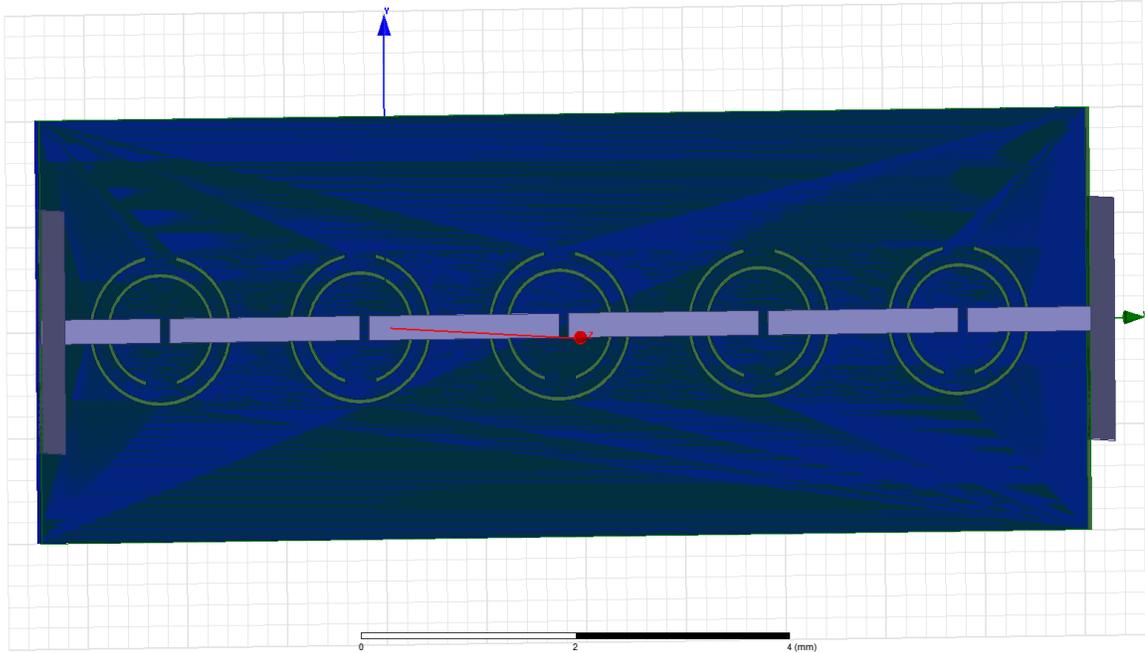
Figure 8.3a. Planar band pass filter design
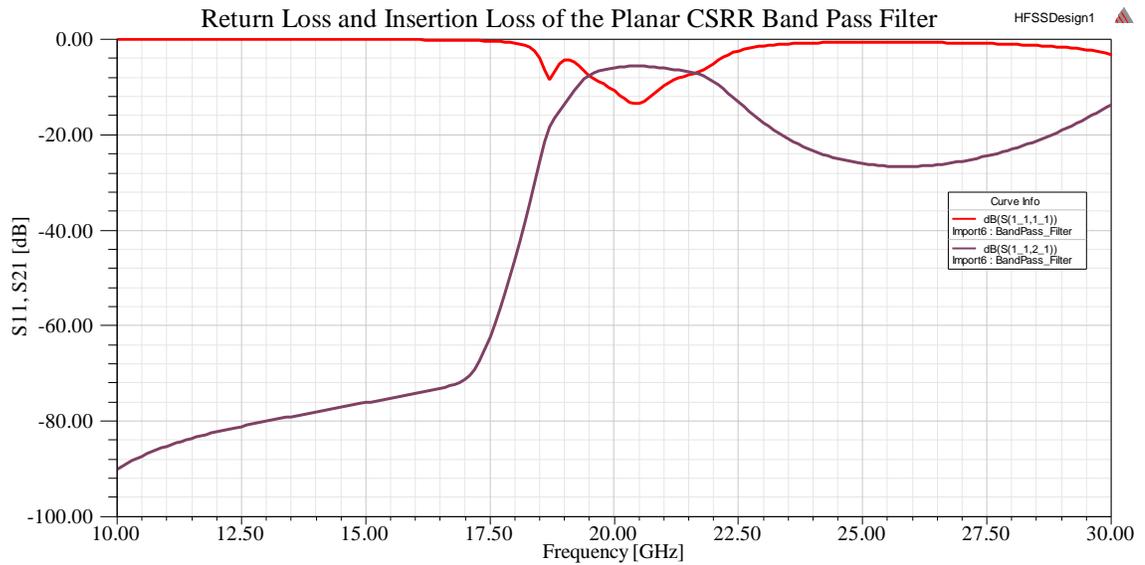
Figure 8.3b. Return loss (red) and insertion loss (purple) results of the band pass filter

The next set of filter images and their simulated results contains the curved

structures. Figure 8.4 is a depiction of the curved high pass filter design along with its

insertion loss and return loss. The depiction shows both the top and bottom sides of the

filter. The filter discerns high frequencies at 18 GHz. The insertion loss of the high pass

component operates at -2 dB.
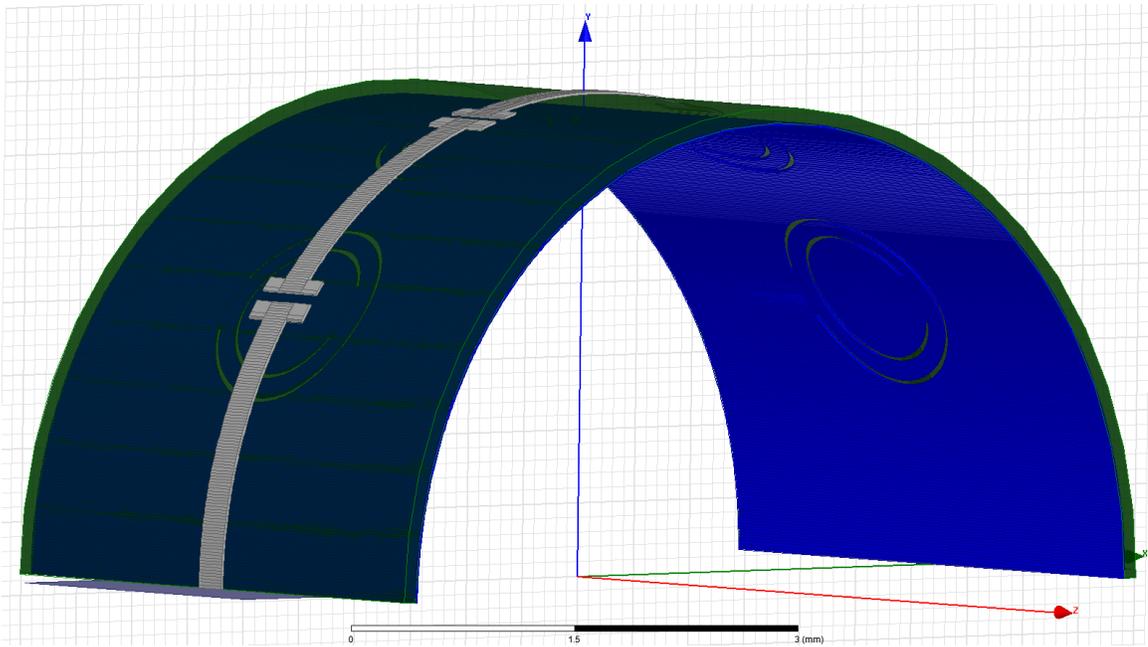
Figure 8.4a. Curved high pass filter design
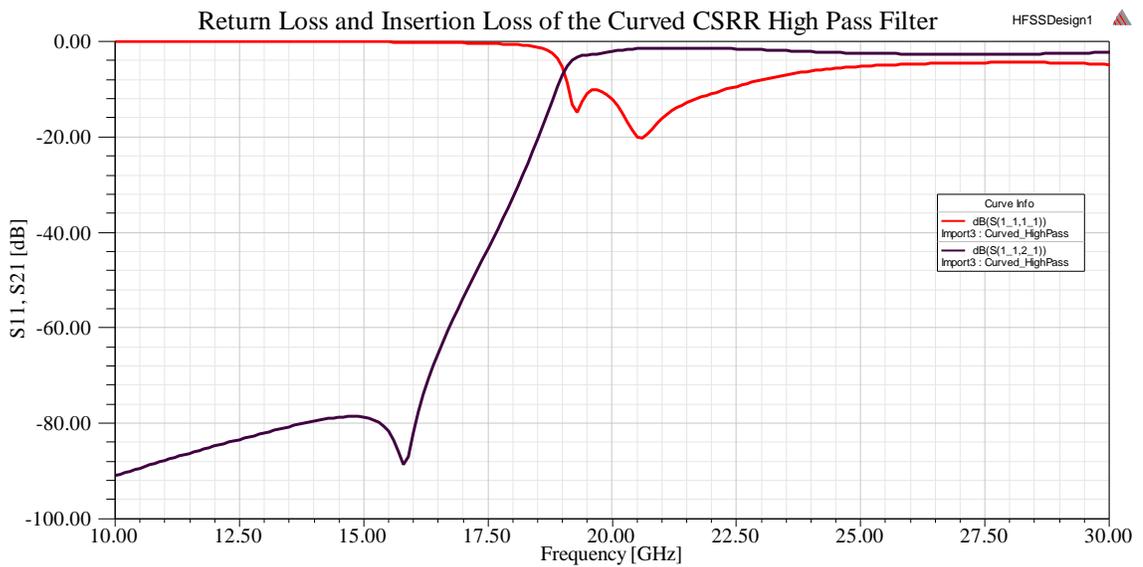
Figure 8.4b. Return loss (red) and insertion loss (purple) results of the curved high pass filter

Figure 8.5 shows the curved band stop filter design along with its insertion loss and return loss. The depiction again shows portions of both the top and bottom sides of the filter. The stop band is between 22 GHz and 26 GHz.
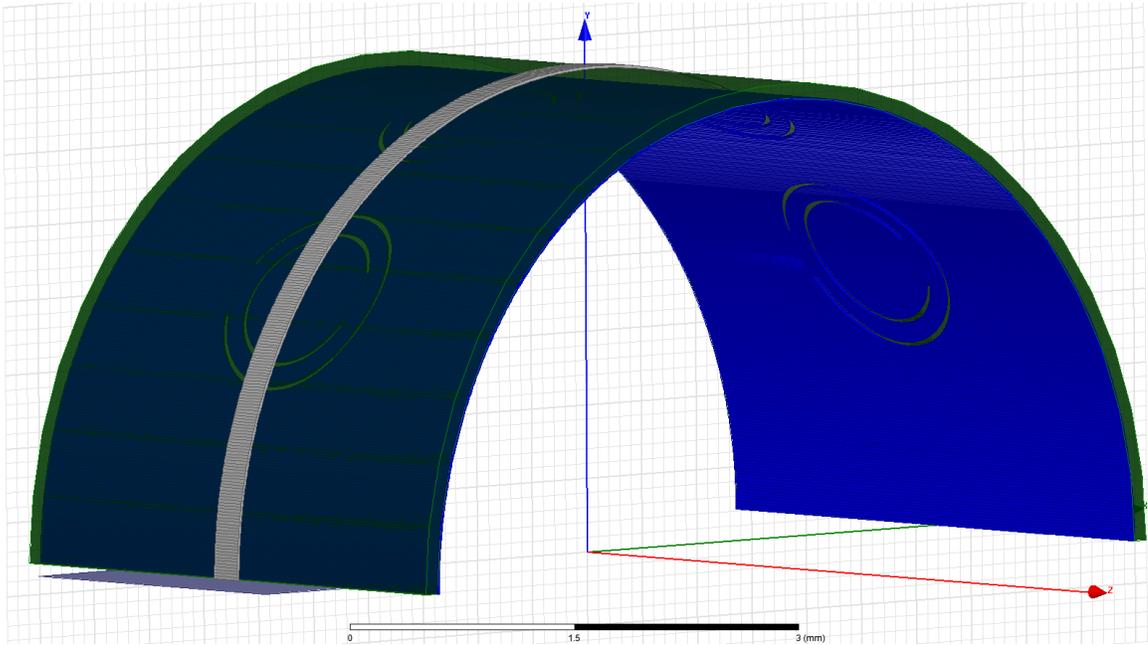

Figure 8.5a. Curved band stop filter design
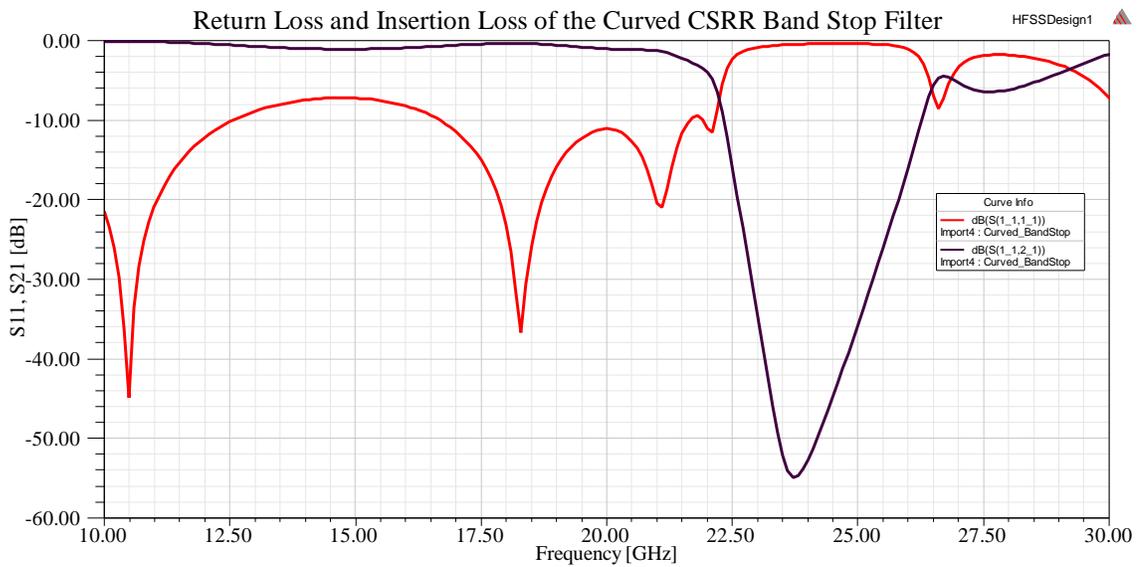
Figure 8.5b. Return loss (red) and insertion loss (purple) results of the curved band stop filter

Figure 8.6 shows the curved band pass filter design along with its insertion loss and return loss. The depiction, like the two above, shows portions of both the top and bottom sides of the filter. The stop band is between 22 GHz and 25 GHz.
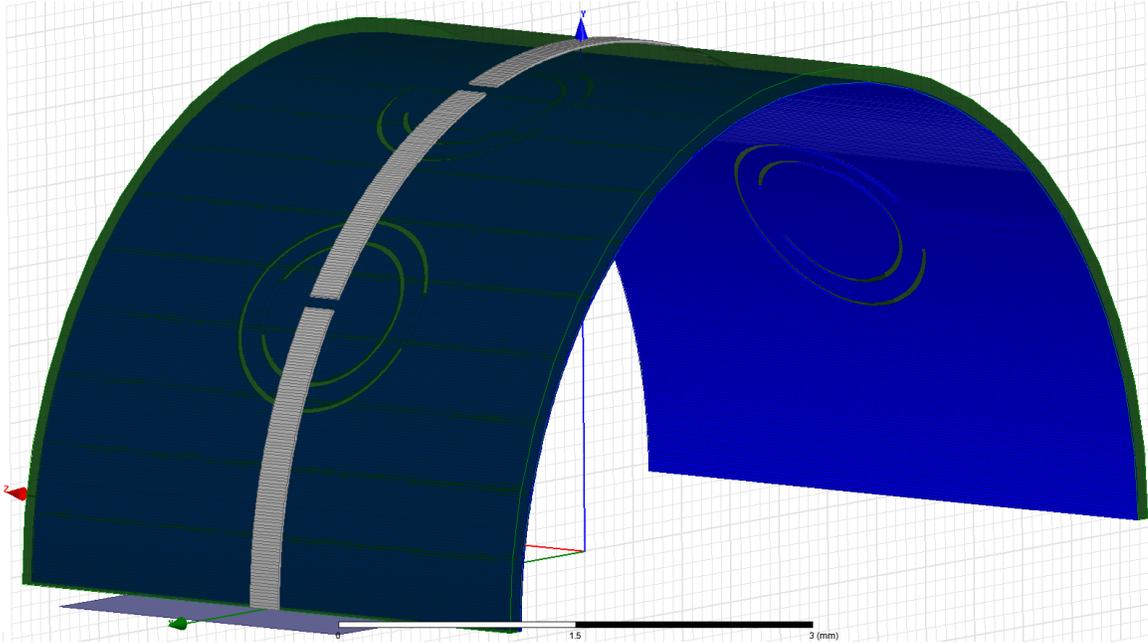

Figure 8.6a. Curved band pass filter design
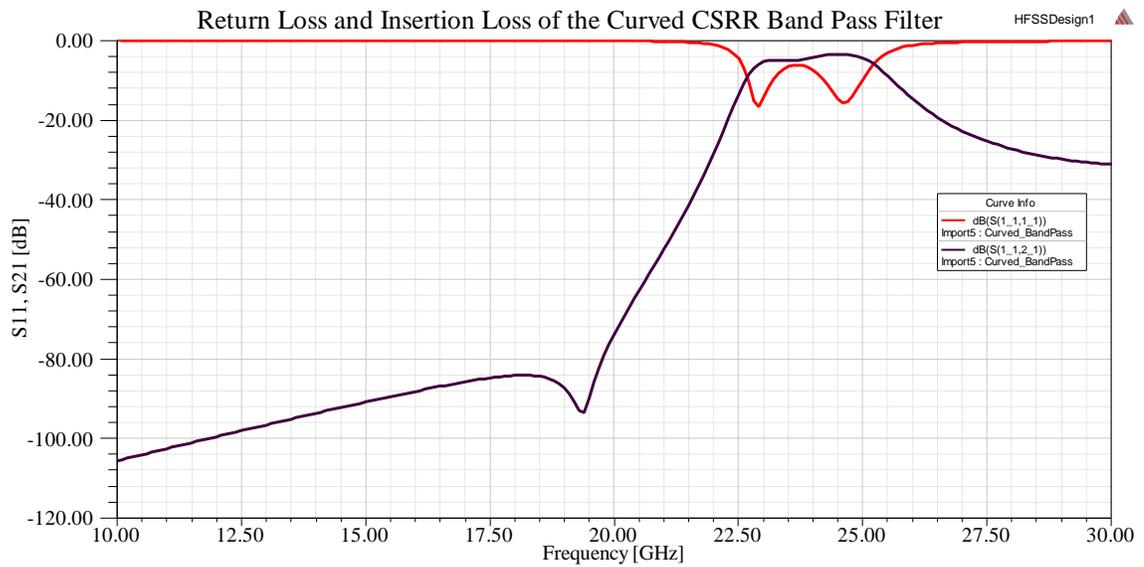
Figure 8.6b. Return loss (red) and insertion loss (purple) results of the curved band pass filter

Comparing the planar structures and curved structures quantitatively helps to discover whether or not the flexible liquid crystal polymer substrate will actually render results in the curved structures that are akin to those in the planar structures. The figures below show the comparative insertion losses of a particular filter's planar and curved structures.
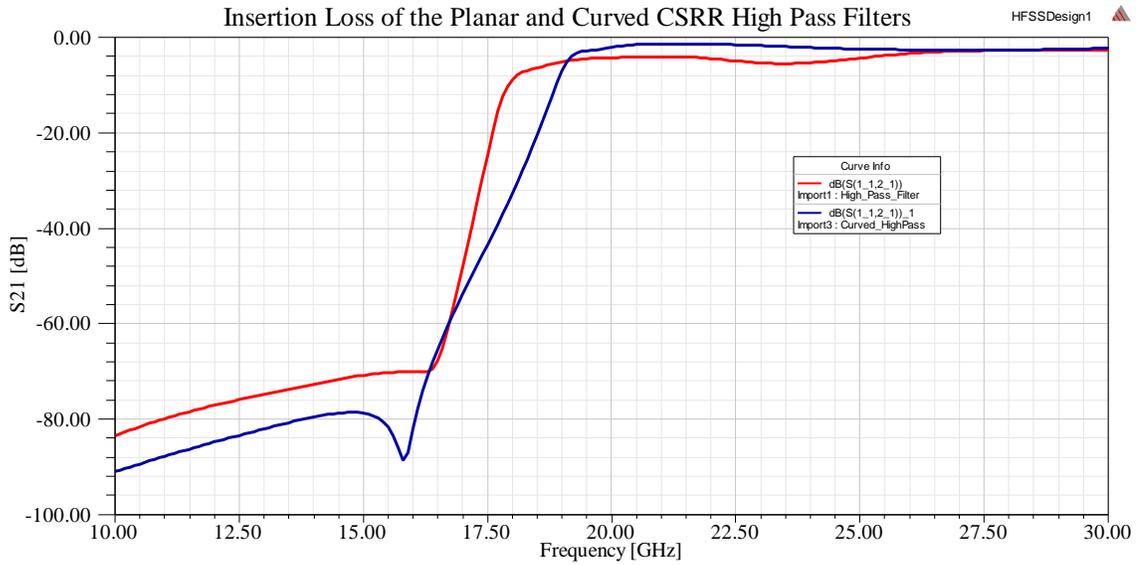
Figure 8.7a. Insertion losses of the planar (red) and curved (blue) high pass filters
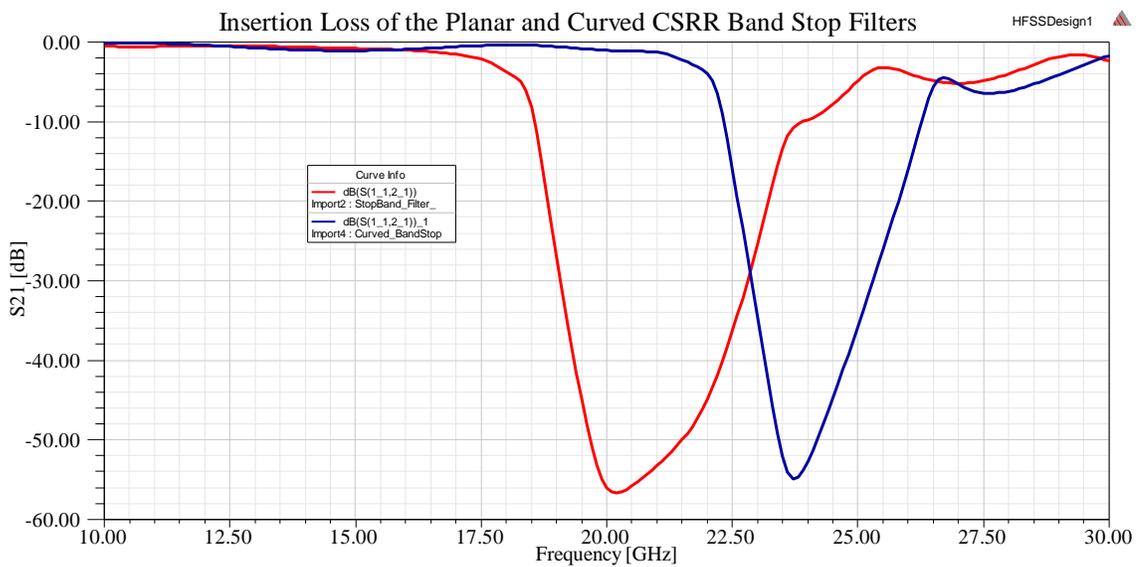
Figure 8.7b. Insertion losses of the planar (red) and curved (blue) band stop filters
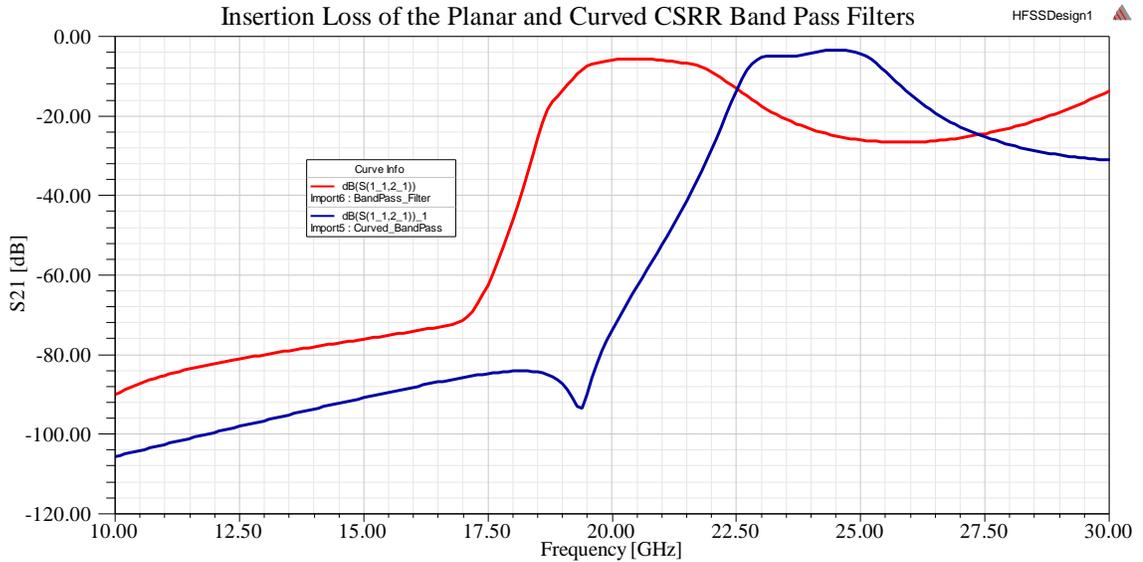
Figure 8.7c. Insertion losses of the planar (red) and curved (blue) band pass filters

The curves used to compare each planar structure to its curved counterpart show that each curve looks similar, but the curved structures are shifted approximately 2.5 GHz-4 GHz higher than the planar structures. This could be attributed to the meshing geometries used in HFSS to actually simulate the curved structures, because in [23], when actual measurements were made on a fabricated band pass structure, the frequency response of the curved filter was similar to its planar form. The discrepancy can also be a result of the inexact geometric calculations that were made to build the structures. Many approximations had to be made.

Conclusions

Designing metamaterial based transmission line filters that are loaded with complementary split ring resonators has been proven to result in robust high frequency filters of varying types. The ones presented in this discussion were decided upon based on the availability of relevant information and simplicity of design, particularly in the case of the curved structures.

Studying HFSS led to the ability to simulate both planar and curved structures. Although the results between the two sets of structures vary by a few GHz, the most plausible explanation is due to the slight errors in the curved structures' geometries and in the HFSS geometric meshing operations.

As was seen above, completing the curved structures is a fairly complex process, which requires some margin of error. The sensitivity of the filters and their CSRRS was also mentioned above. Because many of the geometric measurements were approximated for the sake of simplicity and time, minor adjustments in the design lead to some differences in the scattering parameters.

Performing a metamaterial simulation is also sufficiently taxing on the software's finite element solvers and the computer hardware, but performing similar simulations on less than simple geometries requires advanced meshing and solving techniques.

Even when the discrepancies mentioned above are accounted for, the ability of the flexible liquid crystal polymer substrate to return similar results for both planar and curved filtering structures has been confirmed.

Future Work

Of course this work is another stepping stone to realizing the elusive invisibility cloak, but the most crucial step in developing more advanced metamaterial structures is studying and understanding the simulation software that will be used to model them.

HFSS is capable of running multiple types of simulations beyond the driven modal transmission line simulations produced above. It is capable of performing optimization analyses across several parametric sweeps. The key to this is defining variables and altering them with each successive sweep. These variables are typically related to a structure's geometry.

Beyond parametric sweeps of a structure's geometry, HFSS is also useful in sweeping material parameters. By exploiting that, a user could quite possibly monitor the effects of another flexible material substrate, like polyimide, or even evaluate a different type of metal in a design.

The most significant leap to make from this work revolves around the encouraging results of the differences in the scattering parameters between the planar structures and the curved structures, even though the results did not align perfectly due to the geometric approximations made during the construction of the curved surfaces. The encouragement stems from the realization that a miniscule size difference in the CSRRs,

on the order of 10-50 μm, was enough to shift the frequency response by as much as 4 GHz.

That sizeable shift in frequency due to such a small change speaks to the structures' sensitivity and suggests that tuning could be used to account for filtering specific and unique frequencies across the entire 288 THz visible light spectrum, instead of the need to construct a single device that is tasked with filtering the entire range of optical frequencies. When the research has advanced so far, even generating an invisibility cloak that could be simulated in HFSS could become a reality.

REFERENCES

[1] Encyclopaedia Britannica, "Michael Faraday," Encyclopaedia Britannica Inc. , 2014.

[2] Encyclopaedia Britannica, "James Clerk Maxwell," 2014.

[3] A. Altland, "Classical Electrodynamics".

[4] Encyclopaedia Britannica, "James Clerk Maxwell," Encyclopaedia Britannica Inc., 2014.

[5] T. H. Hand, "Applications of Metamaterials in the Microwave Regime," 2008.

[6] V. Veselago, "The Electrodynamics of Substances with Simultaneously Negative Values (epsilon) and (mu)," *SOVIET PHYSICS USPEKHI,* vol. 10, no. 4, pp. 509-514, January-Febrary 1968.

[7] Z. Duan, B.-I. Wu, S. Xi, H. Chen, M. Chen, "Research Progress in Reversed Cherenkov Radiation in Double-Negative Metamaterials," *Progress in Electromagnetics Research,* pp. 75-87, 2009.

[8] David. R. Smith, John B. Pendry, "Reversing Light With Negative Refraction," *Physics Today,* pp. 37-43, June 2004.

[9] Yuandan Dong, Tatsuo Itoh, "Metamaterial-Based Antennas," *Proceedings of the IEEE,* vol. 100, no. 7, pp. 2271-2285, July 2012.

[10] L. J. Wu Jingfang, "Compact Patch Antenna for WiMAX Application," *IEEE,* pp. 443-445, 2013.

[11] Hisham Assi, "Acoustic Metamaterials: Theory and Potential Applications".

[12] Willam. N. Yunker, Colin B. Stevens, George T. Flowers, Robert N. Dean, "Sound Attenuation Using Microelectromechanical Systems Fabricated Acoustic Metamaterials," *Journal of Applied Physics,* vol. 113, no. 2, 2013.

[13] Pekka Alitalo, Sergei Tretyakov, "Electromagnetic Cloaking with Metamaterials," *Materials Today,* vol. 12, no. 3, pp. 22-29, March 2009.

[14] D. Schurig, J. J. Mock, B. J. Justice, S. A. Cummer, J. B. Pendry, A.F. Starr, D. R. Smith, "Metamaterial Electromagnetic Cloak at Microwave Frequencies," *Science,* vol. 314, pp. 977-980, 10 November 2006.

[15] J. Pendry, "Metamaterials and the Control of Electromagnetic Fields," 2007.

[16] Ricardo Marques, Ferran Martin, Mario Sorolla, Metamaterials with Negative Parameters: Theory Design, and Microwave Applications, K. Chang, Ed., Hoboken, New Jersey: John Wiley and Sons, Inc., 2008.

[17] Juan D. Baena, Jordi Bonache, Ferran Martin, Ricardo Marques Sillero, Francisco Falcone, Txema Lopetegi, Miguel A. G. Laso, Joan Garcia-Garcia, Ignacio Gil, Maria Flores Portillo, Mario Sorolla, "Equivalent-Circuit Models for Split-Ring Resonators and Complementar Split-Ring Resonators Coupled to Planar Transmission Lines," *IEEE Transactions on Microwave Theory and Techniques,* vol. 53, no. 4, pp. 1451-1461, April 2205.

[18] D. R. Smith, Willie J. Padilla, D.C. Vier, S.C. Nemat-Nasser, S. Schultz, "Composite Medium with Simultaneously Negative Permeability and Permittivity," *Physical Review Letters,* vol. 54, no. 18, pp. 4184-4187, 1 May 2000.

[19] Ricardo Marques, Francisco Mesa, Jesus Martel, Francisco Medina, "Comparative Analysis of Edge- and Broadside-Coupled Split Ring Resonators for Metamaterial Design-Theory and Experiments," *IEEE Transactions on Antennas and Propagation,* vol. 51, no. 10, pp. 2572-2581, October 2003.

[20] M. Gil, J. Bonache, F. Martin, "Metamaterial Filters: A Review," *Metamaterials,* vol. 2, no. 4, pp. 186-197, December 2008.

[21] P. Mondal, M. K. Mandal, A. Chaktabarty, S. Sanyal, "Compact Bandpass Filters with Wide Controllable Fractional Bandwidth," *IEEE Microwave and Wireless Components Letters,* vol. 16, no. 10, pp. 540-542, October 2006.

[22] Rakesh Singh Kshetrimayum, Sridhar Kallapudi, SS Karthikeyan, "Stopband Characteristics for Periodic Patterns of CSRRs in the Ground Plane," *IETE Technical Review,* January 2007.

[23] J. T. Richard, "Metamaterial Filters on LCP Substrate Using MEMS Technology," Auburn, AL, 2011.

[24] Ansys Corporation, *HFSS Online Help.*

[25] Xuefeng Wang, Jonathan Engel, Chang Liu, "Liquid Crystal Polymer (LCP) for MEMS: Processes and Applications," *Journal of Micromechanics and Microengineering,* pp. 628-633, 2003.

[26] Robert Neal Dean, Jennifer Weller, Mike J. M. J. Bozack, Chad L. Rodekhor, Brian Farrell, Linas Jauniskis, Joseph Ting, David J. Edell, Jamille F. Hetke, "Realization of Ultra Fine Pitch Traces on LCP Substrates," *IEEE Transactions on Components and Packaging Technologies,* vol. 31, no. 2, pp. 315-321, June 2008.